

The evolution of the cluster X-ray scaling relations in the WARPS sample at $0.6 < z < 1.0$.

B. J. Maughan,^{1,2*}† L. R. Jones,¹ H. Ebeling,³ and C. Scharf⁴

¹*School of Physics and Astronomy, The University of Birmingham, Edgbaston, Birmingham B15 2TT, UK.*

²*Harvard-Smithsonian Center for Astrophysics, 60 Garden St, Cambridge, MA 02140, USA.*

³*Institute for Astronomy, 2680 Woodlawn Drive, Honolulu, HI 96822, USA.*

⁴*Columbia Astrophysics Laboratory, MC 5247, 550 West 120th St., New York, NY 10027, USA.*

23 May 2019

ABSTRACT

The X-ray properties of a sample of 11 high-redshift ($0.6 < z < 1.0$) clusters observed with *Chandra* and/or *XMM-Newton* are used to investigate the evolution of the cluster scaling relations. The observed evolution of the L – T and M – L relations is consistent with simple self-similar predictions, in which the properties of clusters reflect the properties of the universe at their redshift of observation. When the systematic effect of assuming isothermality on the derived masses of the high-redshift clusters is taken into account, the high-redshift M – T and M_g – T relations are also consistent with self-similar evolution. Under the assumption that the model of self-similar evolution is correct and that the local systems formed via a single spherical collapse, the high-redshift L – T relation is consistent with the high- z clusters having formed at a significantly higher redshift than the local systems. The data are also consistent with the more realistic scenario of clusters forming via the continuous accretion of material.

The slope of the L – T relation at high-redshift ($B = 3.29 \pm 0.38$) is consistent with the local relation, and significantly steeper than the self-similar prediction of $B = 2$. This suggests that the non-gravitational processes causing the steepening occurred at $z \gtrsim 1$ or in the early stages of the clusters’ formation, prior to their observation.

The properties of the intra-cluster medium at high-redshift are found to be similar to those in the local universe. The mean surface-brightness profile slope for the sample is $\beta = 0.66 \pm 0.05$, the mean gas mass fractions within $R_{2500(z)}$ and $R_{200(z)}$ are 0.073 ± 0.010 and 0.12 ± 0.02 respectively, and the mean metallicity of the sample is $0.28 \pm 0.16 Z_{\odot}$.

Key words: cosmology: observations – galaxies: clusters: general – galaxies: high-redshift – intergalactic medium – X-rays: galaxies

1 INTRODUCTION

A simple and useful model to describe galaxy clusters is that they are self-similar. In this model, clusters form via the collapse of the most overdense regions in the early universe, and the cluster baryons are heated only by gravitational processes (compression and shock heating) during the collapse. The properties of clusters at high redshift are then identical to those of their low-redshift counterparts, apart from scaling factors reflecting the increase of the mean density of the universe with redshift. This scaling with redshift has been termed weak self-similarity (*e.g.* Bower 1997). In the

strongest form of the model, the mass profiles of all clusters at the same epoch follow the same shape independent of their total mass. The self-similar model then allows properties of clusters of different masses and at different redshifts to be related to one-another according to simple scaling laws.

X-ray observations provide a powerful way of measuring cluster properties, and have provided a wealth of evidence that galaxy clusters do not scale self-similarly with mass (or, by proxy, temperature) in the local universe. For example; the slope of the X-ray luminosity-temperature (L – T) relation is steeper than self-similar predictions (*e.g.* Markevitch 1998; Arnaud & Evrard 1999); the slopes of the gas-density and surface-brightness profiles are shallower in cooler systems (*e.g.* Lloyd-Davies et al. 2000; Sanderson et al. 2003); and the entropy in cluster cores is higher than predicted

* E-mail: bmaughan@cfa.harvard.edu

† Chandra Fellow

(*e.g.* Ponman et al. 1999, 2003). These departures from self-similarity are generally taken as evidence for the importance of non-gravitational contributions (such as heating by AGN or radiative cooling) to the energy budget of clusters.

In this paper we address the open question of whether the simple evolution with redshift of the cluster scaling relations predicted by the self-similar model is obeyed. The results of early studies of the evolution of the L – T relation were consistent with little or no evolution (*e.g.* Mushotzky & Scharf 1997; Donahue et al. 1999; Fairley et al. 2000). More recent studies with *Chandra* and *XMM-Newton* have found significant evolution in the L – T relation (Vikhlinin et al. 2002; Ettori et al. 2004; Lumb et al. 2004). This change is due to the availability of larger samples of clusters at higher redshifts, and differences in the assumed cosmological model. The measured evolution is larger in a Λ CDM cosmology than in the Einstein de-Sitter models which were assumed in many of the earlier studies (*e.g.* Arnaud et al. 2002; Lumb et al. 2004).

Here we present an analysis of a sample of 11 clusters in the redshift range $0.6 < z \leq 1.0$ drawn from the Wide Angle *ROSAT* Pointed Survey (WARPS: Scharf et al. 1997; Perlman et al. 2002). An almost complete, flux-limited sample of 12 WARPS clusters was originally observed with *Chandra* and/or *XMM-Newton*, but one of the *XMM-Newton* observations were rendered unusable due to extremely high background levels, leaving the 11 clusters discussed here. These clusters’ properties, and the scaling relations derived from them, are compared to those of other samples at high and low redshift, and with the predictions of different cluster-formation models.

A Λ CDM cosmology of $H_0 = 70 \text{ km s}^{-1} \text{ Mpc}^{-1} \equiv 100h_{70} \text{ km s}^{-1} \text{ Mpc}^{-1}$, and $\Omega_M = 0.3$ ($\Omega_\Lambda = 0.7$) is adopted throughout, with the convention that Ω_M represents the present-day matter density, while $\Omega_m(z)$ represents its value at redshift z . All errors are quoted at the 68% level.

2 DATA ANALYSIS

The standard data reduction steps were followed for both the *Chandra* and *XMM-Newton* observations, and are discussed in detail in Maughan et al. (2003) (*Chandra*) and Maughan et al. (2004a) (*XMM-Newton*). In summary, the data were filtered to remove high-background periods, and a surface-brightness profile was extracted (with point sources excluded) to determine the extent of the cluster emission. The detection radius (r_a) of the cluster was then defined as the radius outside which no further emission was detected at the 3σ level in the surface-brightness profile. Spectra were extracted from within the detection radius, and were fit in the 0.5 – 5 keV band with an absorbed MEKAL model (Kaastra & Mewe 1993), with the absorption frozen at the Galactic value determined from 21 cm radio observations (Dickey & Lockman 1990). The surface-brightness distribution of each system was modeled with a two-dimensional β -model (Cavaliere & Fusco-Femiano 1976).

The issue of background subtraction was carefully considered when modeling both the spectra and the surface-brightness distributions. In all cases the background was measured from the same observation in a region as close to the source as possible, while avoiding contaminating source

emission. Due to the higher background levels in the *XMM-Newton* observations, the background in the *XMM-Newton* surface-brightness models included two components to account for the flat and vignetted background components (Maughan et al. 2004a). Consistency checks were performed for several clusters from the sample using backgrounds derived from different regions of the source datasets and from blank-sky datasets (*e.g.* Maughan et al. 2003; Maughan et al. 2004a). The derived properties were generally independent of the background used. Point sources were masked out from all source and background regions during the analyses.

During the spectral-fitting process, the model redshifts were frozen at the values derived from optical spectroscopy, and best-fitting temperatures were found with the metallicity (Z) fixed at $0.3Z_\odot$. The metallicity parameter was then allowed to vary in addition to the model temperature and normalisation, and its best-fitting value was found. In all cases, the best-fitting model temperatures obtained with and without the metallicity free to vary agreed within 1σ . As the metallicities were not always well constrained, the temperatures derived with metallicity fixed at $0.3Z_\odot$ are used throughout this work. The effective area of the instruments was taken into account in the spectral modeling by using ancillary response files (ARFs) generated for the cluster positions, and weighted by the spatial distributions of source photons.

For the purposes of spectral fitting, additional filtering was applied to the *XMM-Newton* data retaining only events with FLAG and PATTERN parameters equal to zero. These correspond to events detected in single pixels which were not close to CCD gaps. The energy calibration of these events is the most reliable. The loss of effective area to CCD gaps, bad pixels, and excluded point sources within the spectral extraction region was accounted for by correcting the normalisation of the ARFs. While the ARF files already account for these losses in principal, they do not take into account the surface brightness distribution of the source. We included this effect in our correction as follows. For each cluster, a background-subtracted radial profile of the source region was produced, excluding “dead regions” (CCD gaps, bad pixels and point sources). In each radial bin, the measured flux was used to predict the number of counts that would have been detected if there were no dead regions. These counts were summed over the source region, and the ARF normalisation was scaled by the ratio of the detected counts to the predicted total counts if there were no dead regions. This process was not required for the *Chandra* observations as the spectral extraction regions were unaffected by dead regions. The spectral redistribution matrix files were generated with with the *XMM-Newton* Science Analysis Software (SAS) version 6.1 using the calibration database appropriate for that release, which included improved calibration of the PN response at low energies.

For the three clusters observed with *Chandra* (see Table 1), two other corrections were made to the ARF files. They were constructed with the calibration database version 2.26 to correct for the degradation in the ACIS quantum efficiency¹. In addition, as the observations were taken with the ACIS-I array, the ARFs were manually corrected to reduce

¹ see <http://xc.harvard.edu/ciao/threads/aciscontam>

the effective area below 1.8 keV by 7% (see Markevitch & Vikhlinin 2001). This introduces some uncertainty ($\sim 7\%$) in the normalisation of the spectral models, but improves the reliability of the temperature measurement (see *Chandra* help-desk ticket #6802). The best-fitting temperature of all three systems was reduced by 0.2 – 0.3 keV by the second correction.

All of the clusters in our sample, with the exception of ClJ0046.3+8530, were the target of their observations and were located close to the optical axis. However ClJ0046.3+8530 was observed serendipitously near the edge of the field of view in two *XMM-Newton* observations, which introduced some additional calibration issues due to the broader PSF. The analysis of this system is discussed in detail in Maughan et al. (2004b).

The slope (β) and core radius (r_c) of the gas-density profile were derived from a two-dimensional elliptical β -model fitted to an image of the cluster emission, including the effects of vignetting and the PSF. The ellipticity of the model was defined as $e = (1 - b/a)$, where a and b are the semi-major and -minor axes respectively. With the central gas density derived from the normalisation of the best-fitting spectral model (e.g. Maughan et al. 2003), it was then possible to derive the gas-mass profile assuming spherical symmetry. The total mass profile was then derived under the assumptions of isothermality, hydrostatic equilibrium, and spherical symmetry. From this total mass profile, an overdensity profile (with respect to the critical density $\rho_c(z)$ at the cluster’s redshift) was derived, enabling the measurement of overdensity radii, R_Δ . Here R_Δ refers to the radius within which the mean density is $\Delta\rho_c(z)$, and Δ is an overdensity factor. We take Δ to be a function of redshift, as explained in §4, and denote radii defined in this way as e.g. $R_{200(z)}$ where $\Delta = 200$ at $z = 0$.

2.1 Computation of errors

The uncertainties on the derived properties of a cluster were obtained in the following way. Distributions of the derived properties were computed from 10,000 randomisations of the observed properties within their uncertainty distributions. The 1σ confidence limits on each of the derived properties were then obtained from the ± 34 percentiles about the best-fit value. This method treats the statistical uncertainties in extrapolating properties to different radii self-consistently, but does not account for any systematic uncertainties in extrapolating properties beyond the limits of the data. A significant source of systematic uncertainty is the assumption of isothermality. Data of sufficient quality to measure temperature profiles were only available for two clusters in the sample, but in those cases the assumption of isothermality was justified. The systematic effect that undetected temperature gradients have on derived masses is discussed in §7 and §8.

An additional consideration is the well known positive correlation between the β and r_c surface-brightness profile parameters. Models with large β and r_c are similar to those with small values of the parameters. The error treatment described above assumes that all errors are independent. The effect of this assumption was investigated in the following way: A simple cluster image was simulated by adding Poisson noise to a two-dimensional β -profile image. A β -

model was then fit to this image, and a two-dimensional probability distribution of β and r_c values was generated. Cluster properties were then derived for an assumed temperature and MEKAL normalisation, and the uncertainties were computed by sampling pairs of β and r_c values from the two-dimensional probability distribution, thereby accurately reflecting their correlated errors. The uncertainties on all other parameters were assumed to be negligible. This process was repeated assuming uncorrelated β and r_c errors, and also assuming negligible errors on r_c . It was found that the latter two methods gave similar uncertainties on cluster properties, and these uncertainties were approximately twice as large as those derived using the true, correlated errors on β and r_c . In fact, the uncertainties on the properties of the observed clusters are dominated by the measurement errors on the temperature, and the choice between these methods makes a negligible contribution to the error budget. With this in mind, the measurement errors on r_c were ignored in the calculation of the errors on all cluster properties.

An interesting consequence of this self-consistent treatment of errors is that the fractional uncertainty on R_{2500} is in general significantly larger than that on R_{200} . This is in spite of the fact that the data for all of the clusters extend beyond R_{2500} , but must be extrapolated to R_{200} (see Table 1). The reason for this is that without including any systematic uncertainties due to the extrapolation, the distribution of β values has a larger effect on the shape of the density profile at small radii than large ($\gg r_c$) radii. Fig. 1 illustrates this point, showing a range of 50 overdensity profiles derived for a 5.5 keV cluster at $z = 0.833$ with $r_c = 250$ kpc and values of β randomly drawn from the distribution 0.67 ± 0.07 . These uncertainties on β are the average fractional uncertainties on our sample, and so reflect the typical uncertainty in the shape of the overdensity profiles. In these simulations, the fractional error on R_{2500} is 0.11, while that on R_{200} is 0.05. The self-consistent treatment of the uncertainties can thus result in larger fractional error on quantities derived within the extent of the data than those extrapolated to large radii beyond the data. While the measurement errors on kT have a large effect on the uncertainty in the normalisation of the overdensity profiles, this source of uncertainty is not important for this comparison as it does not affect the shape of the profiles.

3 THE SAMPLE

In this section each cluster in the sample is discussed briefly, highlighting any unusual or interesting aspects of its analysis and properties. Images of each of the clusters with contours of the adaptively smoothed X-ray emission overlaid are shown in Fig. 2 and the observed properties of the sample are summarised in Table 1 in redshift order. The detection radii of each cluster as a fraction of $R_{2500(z)}$ and $R_{200(z)}$ are also given in Table 1. The method used to define and measure these overdensity radii is described in §4 and their values are given in Table 2 for each cluster.

ClJ0046.3+8530. This cluster was observed serendipitously 11’ off axis in two consecutive *XMM-Newton* observations of the open star cluster NGC 188. These data are discussed in detail in Maughan et al. (2004b). The cluster has a reasonably relaxed morphology, and its temperature

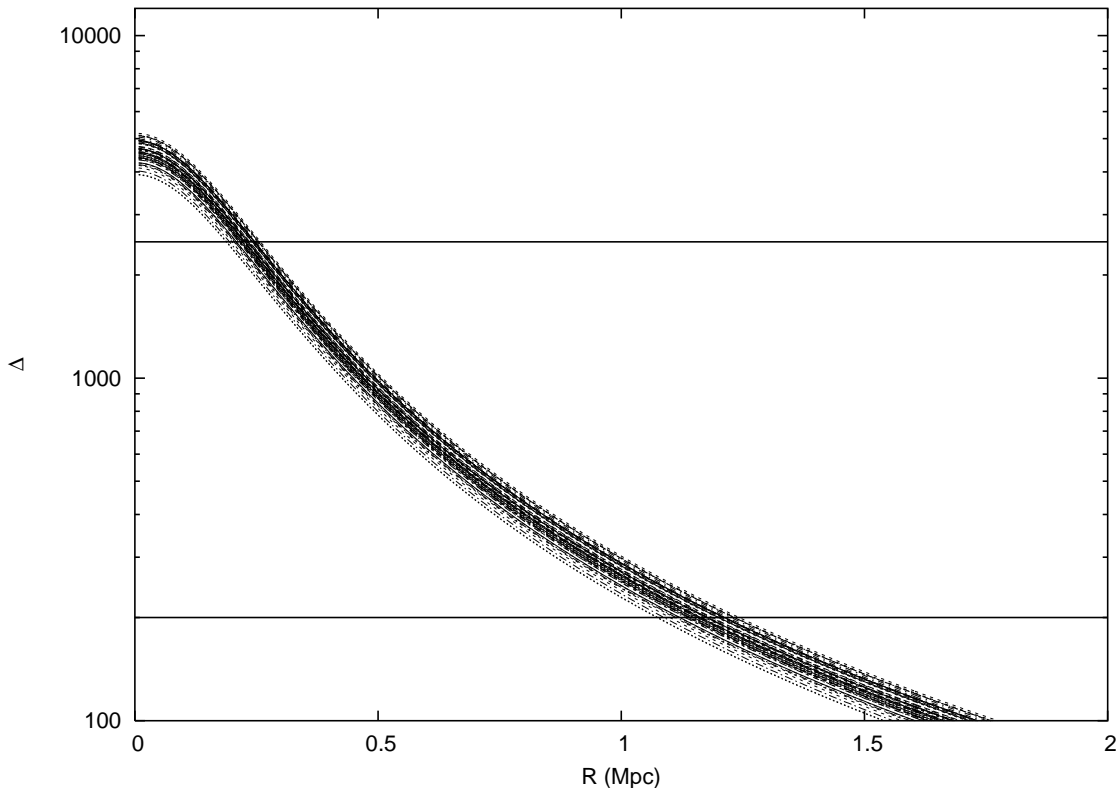


Figure 1. 50 sample overdensity profiles generated for a distribution of β values. The horizontal lines mark overdensities of 200 and 2500. The overdensity at R is defined as the ratio of the mean density within R to the critical density.

profile and hardness-ratio map are consistent with isothermality out to 70% of the virial radius, within the statistical limits of the data.

CIJ1342.9+2828. The *XMM-Newton* observation of this system shows a core region that is elongated in the East-West direction, with two possible X-ray peaks. This morphology is indicative of a late-stage merger.

CIJ1113.1–2615. The *Chandra* observation of this cluster, which is discussed in detail in Maughan et al. (2003), shows a reasonably relaxed, although slightly elliptical, morphology.

CIJ1103.6+3555. Observed with *XMM-Newton*, this cluster has a fairly disturbed X-ray morphology, suggesting that it may not have dynamically relaxed after a recent merger. It also appears to be surrounded by more extended low surface-brightness emission.

CIJ0152.7–1357. This spectacular system is probably an early-stage merger between two equally massive clusters CIJ0152.7–1357N and CIJ0152.7–1357S and has been studied in some detail (Ebeling et al. 2000; Maughan et al. 2003; Huo et al. 2004; Jee et al. 2005). The *Chandra* observation used here suggests that both of the clusters are reasonably relaxed, with CIJ0152.7–1357N the more elliptical. A recent, deep *XMM-Newton* observation has detected some substructure in CIJ0152.7–1357N, while CIJ0152.7–1357S still appears relaxed (Maughan et al. in preparation).

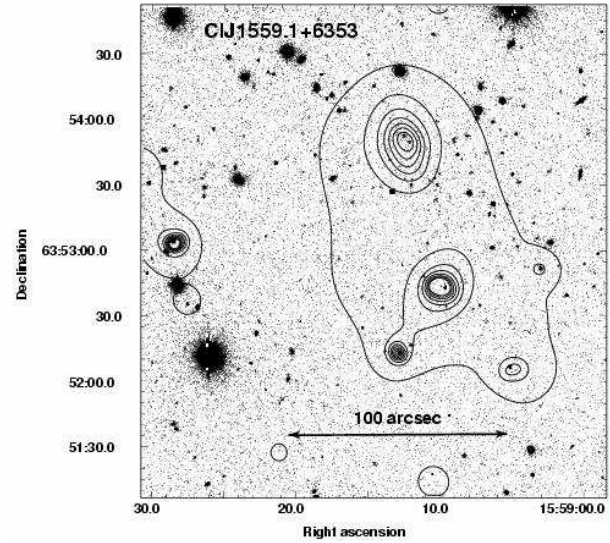
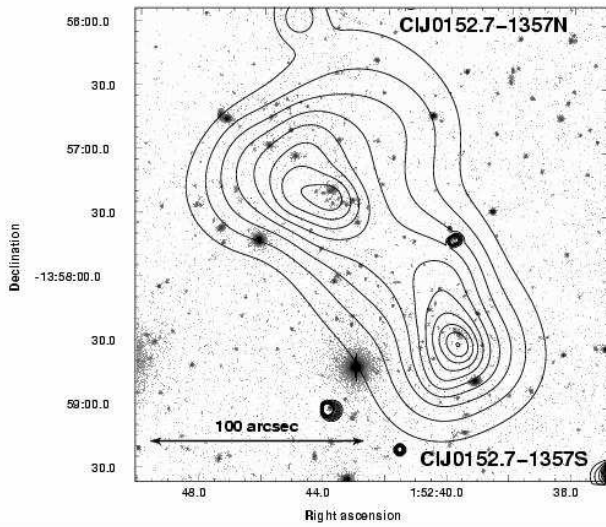
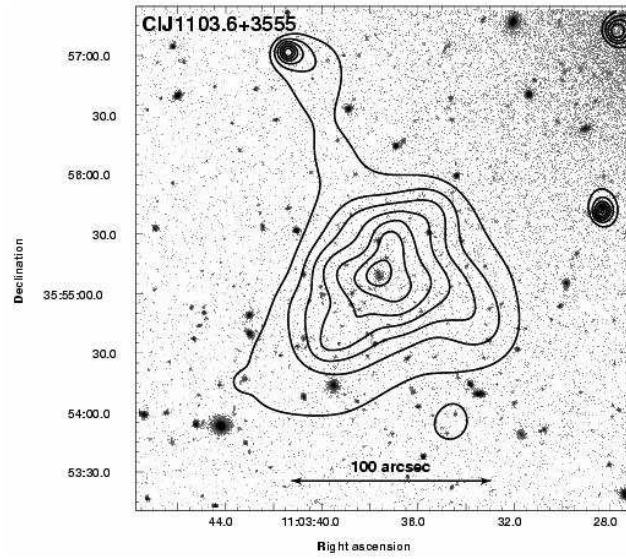
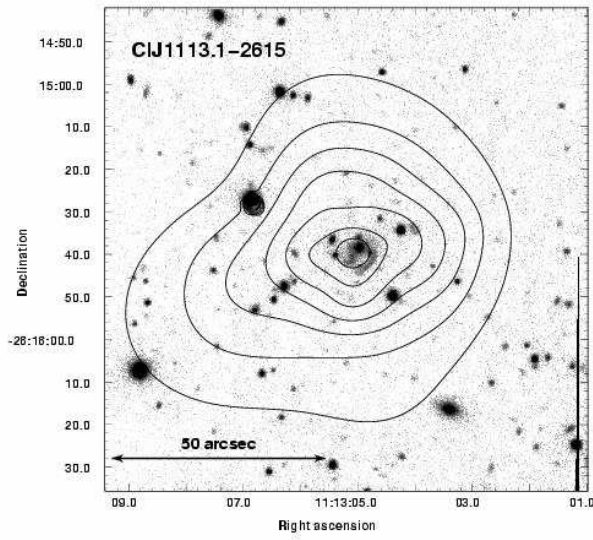
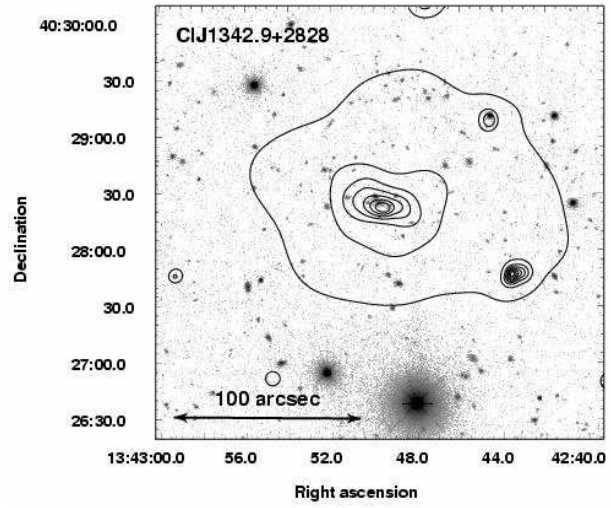
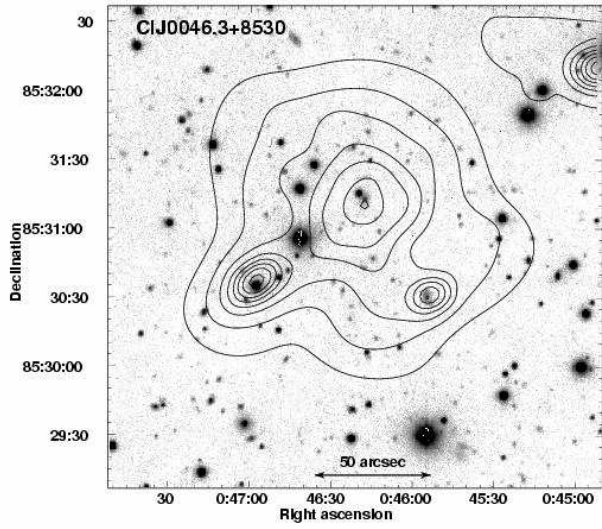
CIJ1559.1+6353. This cluster was observed by *XMM-Newton*. The data show an elliptical morphology ($e = 0.35$; see Table 1), suggesting that the system may not yet have fully relaxed back into hydrostatic equilibrium after its last merger event. A bright, variable point-source $\approx 1'$ South of

the cluster centroid led to an overestimate of its *ROSAT* flux in the WARPS (Horner et al. in preparation). For this system, a very high, poorly constrained metallicity was measured, with relatively poor constraints on temperature (see Table 1). This is likely to be due to some remaining contamination from the bright source caused by the large wings of the *XMM-Newton* point spread function, and to the fact that the spectrum had a lower signal-to-noise than most of the other systems discussed here.

CIJ1008.7+5342. The morphology of this cluster appears fairly relaxed in the *XMM-Newton* observation. However, the ellipticity of the best-fitting surface-brightness model is 0.27, indicating that the system may be disturbed to some degree.

CIJ1226.9+3332. This system has been the target of both *Chandra* (Cagnoni et al. 2001) and *XMM-Newton* (Maughan et al. 2004a) observations, and was found to be extremely hot, with a regular, relaxed morphology. Based on a 16 ks *XMM-Newton* observation Maughan et al. (2004a) measured a temperature profile and hardness-ratio map which were consistent with the cluster being isothermal out to 45% of the virial radius. In addition, the temperature and luminosity measured from the *Chandra* and *XMM-Newton* data were found to be in good agreement (Maughan et al. 2004a). The properties derived from the *XMM-Newton* data are used throughout this work. A forthcoming deep *XMM-Newton* observation will allow this massive cluster to be studied in unprecedented detail.

CIJ1429.0+4241. This cluster was observed serendipitously during an *XMM-Newton* observation of the BL Lac



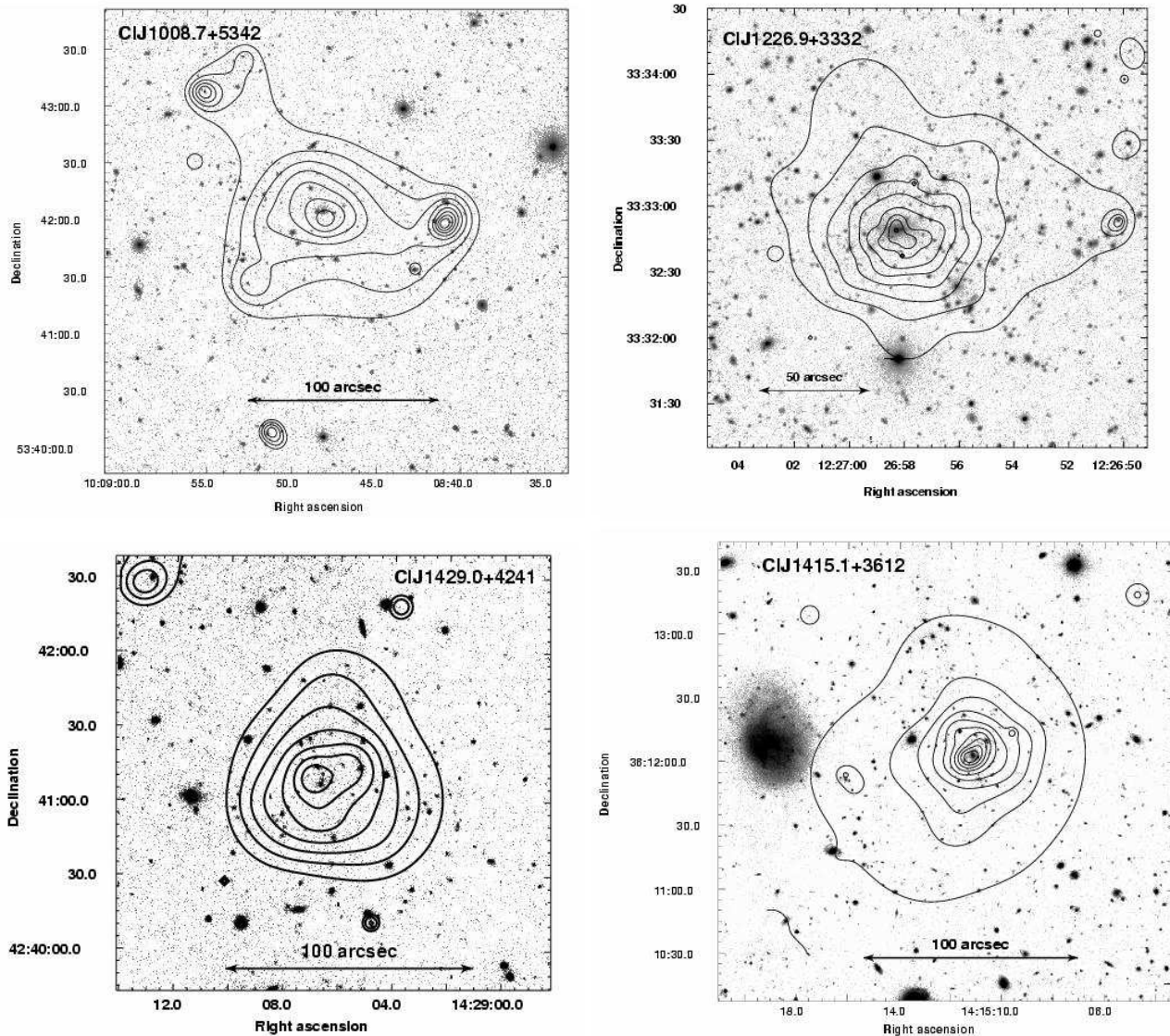


Figure 2. Contours of X-ray emission overlaid on optical images of the WARPS high-redshift sample. The pass-bands and telescopes used to produce the optical images varied, with the I, R or Z band, and Keck-II, the 4.2m William-Herschel Telescope, Subaru or the University of Hawaii’s 2.2m telescope used. Contours are taken from images that were adaptively smoothed such that all features are significant at the 99% level, and are logarithmically spaced, with the lowest contour a factor of 1.5 above the background. The X-ray observatory used, and other information about the clusters is given in Table 1.

H1426+428. Only the data from the MOS2 detector were useful for its study because the other detectors were in fast timing mode. The cluster’s morphology is fairly disturbed, particularly in the centre, with a possible second X-ray peak to the West. During the two-dimensional surface-brightness modeling of this system, it was not possible to constrain the β parameter. This is likely to be due to a combination of the system’s morphology, its compactness compared with the *XMM-Newton* PSF, and the relatively shallow imaging with the single MOS detector. The fit was thus performed with β fixed at the canonical value of 0.67, and the errors quoted on β hereafter are the mean fractional errors of the rest of the sample (9%).

CIJ1415.1+3612. At $z = 1.03$, the most distant cluster in the sample. The *XMM-Newton* data show the morphology to

be relaxed. A deep (78 ks) *Chandra* observation (Ebeling et al. in preparation) of this system confirms the relaxed morphology, and rules out significant unresolved point source contamination in the *XMM-Newton* data used here.

The measurement of reliable masses for these clusters based on the X-ray data requires that they be spherically symmetric and in hydrostatic equilibrium. Five systems (CIJ1342.9+2828, CIJ1103.6+3555, CIJ0152.7–1357N, CIJ1559.1+6353 and CIJ1429.0+4241) are possibly unrelaxed showing disturbed morphologies, possible substructure and/or large ellipticities. These systems were thus excluded from the investigation of the M – T relations (§7 & 8). CIJ1008.7+5342 is possibly a borderline case, which is included in the analysis, but commented on further below.

Cluster	z	satellite	exposure (ks)	r_d^\dagger			scale (kpc/'')	kT (keV)	Z (Z_\odot)	r_c (kpc)	β	e
				('')	($R_{2500(z)}$)	($R_{200(z)}$)						
CIJ0046.3+8530 ^a	0.62	X	44	88	2.5	0.63	6.81	$4.4^{+0.5}_{-0.4}$	$0.60^{+0.22}_{-0.19}$	137^{+30}_{-25}	$0.60^{+0.08}_{-0.03}$	0.07
CIJ1342.9+2828	0.71	X	33	109	4.3	0.89	7.19	$3.7^{+0.6}_{-0.6}$	$0.17^{+0.23}_{-0.17}$	172^{+28}_{-24}	$0.70^{+0.06}_{-0.05}$	0.34
CIJ1113.1–2615 ^b	0.73	C	88	50	1.5	0.40	7.24	$4.1^{+0.5}_{-0.4}$	$0.62^{+0.25}_{-0.22}$	106^{+9}_{-16}	$0.67^{+0.03}_{-0.05}$	0.20
CIJ1103.6+3555	0.78	X	36	95	3.3	0.79	7.43	$5.0^{+0.7}_{-0.6}$	$0.37^{+0.24}_{-0.21}$	141^{+21}_{-16}	0.58 ± 0.03	0.18
CIJ0152.7–1357N ^b	0.83	C	34	49	2.7	0.39	7.61	$5.3^{+0.7}_{-0.7}$	$0.15^{+0.22}_{-0.15}$	249^{+53}_{-33}	$0.73^{+0.13}_{-0.06}$	0.08
CIJ0152.7–1357S ^b	0.83	C	34	37	1.2	0.31	7.61	$4.9^{+1.0}_{-0.9}$	$0.70^{+0.72}_{-0.44}$	123^{+28}_{-20}	$0.66^{+0.08}_{-0.06}$	0.00
CIJ1559.1+6353	0.85	X	19	73	2.6	0.70	7.54	$4.4^{+1.8}_{-1.1}$	$1.57^{+3.70}_{-0.81}$	67^{+34}_{-25}	$0.59^{+0.06}_{-0.11}$	0.35
CIJ1008.7+5342	0.87	X	14	98	4.8	0.95	7.72	$4.0^{+1.0}_{-0.7}$	$0.25^{+0.50}_{-0.25}$	170^{+47}_{-39}	$0.68^{+0.10}_{-0.08}$	0.27
CIJ1226.9+3332 ^c	0.89	X	17	100	2.2	0.59	7.76	$11.1^{+1.5}_{-1.4}$	$0.52^{+0.18}_{-0.18}$	113^{+9}_{-6}	$0.66^{+0.02}_{-0.02}$	0.14
CIJ1429.0+4241	0.92	X	44	50	1.5	0.39	7.84	$6.6^{+2.1}_{-1.7}$	$0.43^{+0.56}_{-0.43}$	97 ± 9	$0.67 \pm 0.06^\ddagger$	0.16
CIJ1415.1+3612	1.03	X	17	60	2.1	0.56	8.06	$5.5^{+1.3}_{-0.8}$	$0.45^{+0.39}_{-0.33}$	94^{+19}_{-14}	$0.67^{+0.06}_{-0.04}$	0.16

Table 1. Summary of the observed properties of the WARPS high-redshift sample. Column 3 indicates whether the observation used here was made with *Chandra* (C) or *XMM-Newton* (X). Column 4 gives the on-axis exposure time remaining after removal of high-background periods (the mean of the MOS and PN times is given for *XMM-Newton* observations). Detailed analyses of several of the clusters can be found in ^aMaughan et al. (2004b), ^bMaughan et al. (2003) and ^cMaughan et al. (2004a). [†]The detection radius is given in units of $R_{2500(z)}$ and $R_{200(z)}$ for each cluster. These radii are defined in §4 and given in Table 2. [‡]The value of β for this cluster was fixed at 0.67 during the surface-brightness fitting, and the error quoted here is the mean fractional error on β in the rest of the sample.

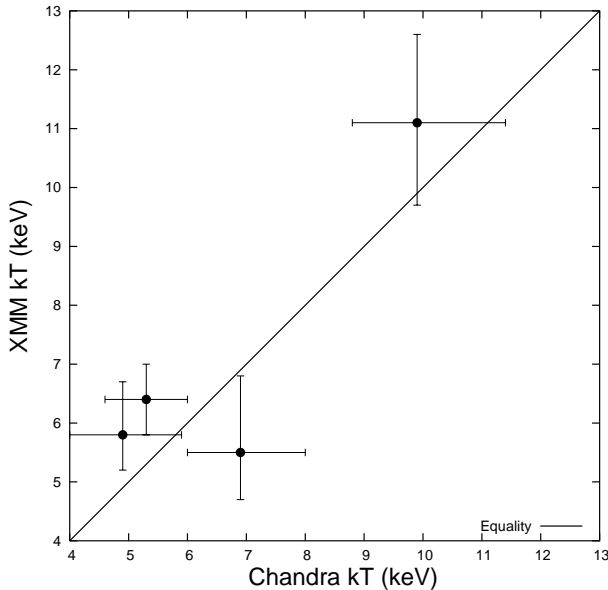


Figure 3. Comparison of temperatures measured with *Chandra* and *XMM-Newton* for the four clusters in our sample observed by both.

3.1 Comparison of *Chandra* and *XMM-Newton* Temperatures

In compiling a sample which includes observations performed with two different instruments, the accuracy of their cross-calibration is an important consideration. In particular, for the study of scaling relations, it is important that no systematic bias in the measured temperature is present due to the imperfect calibration of either instrument. For 4 of the clusters in the sample (CIJ0152.7–1357N, CIJ0152.7–1357S, CIJ1226.9+3332 and CIJ1415.1+3612) observation made with both *Chandra* and *XMM-Newton* were available to us. This enabled us to measure temperatures in a consistent way with both observatories. The measured temperatures are plotted in Fig. 3.

While limited by the small number of comparison points

and the size of the statistical uncertainties on the temperatures, Fig. 3 suggests no gross systematic disagreement between the *Chandra* and *XMM-Newton* temperatures. This evidence, along with the good agreement between the WARPS L – T relation and the *Chandra* L – T relation of Vikhlinin et al. (2002) (discussed in detail in §6.1) indicate that the cross calibration of the two satellite is not a significant problem in this work.

4 CLUSTER SCALING THEORY

When comparing integrated cluster properties such as luminosity and mass with theoretical predictions, simulations, or other work, the radius within which the properties are measured is of great importance. It is common to use a fixed physical size as an outer radius, which has obvious benefits in terms of simplicity. A more sophisticated method is to define a radius with some knowledge of the cluster’s mass profile so that the mean enclosed density is a fixed factor above the critical density of the universe. This method is more appropriate for comparisons with theoretical predictions, which predict the outer boundary of the virialised part of clusters in terms of a density contrast (Δ_v). For instance, in an Einstein-de Sitter universe, the mean density of virialised systems is $\Delta_v = 18\pi^2\rho_c$ at all redshifts (*e.g.* Bryan & Norman 1998). However, the value of Δ_v and its variation with redshift are cosmology dependent (as, of course, is $\rho_c(z)$). Bryan & Norman (1998) calculate the redshift dependence of Δ_v in a Λ CDM cosmology for clusters which have just virialised, fitting the solution with the expression

$$\Delta_v(z) = 18\pi^2 + 82(\Omega_m(z) - 1) - 39(\Omega_m(z) - 1)^2, \quad (1)$$

where $\Omega_m(z) = \Omega_M(1+z)^3/E(z)^2$, and $E(z)$ describes the redshift evolution of the Hubble parameter, given by

$$E^2(z) = \Omega_M(1+z)^3 + (1 - \Omega_M - \Omega_\Lambda)(1+z)^2 + \Omega_\Lambda. \quad (2)$$

Equation 1 is accurate to within 1% in the range $0.1 \leq \Omega(z) \leq 1$ (Bryan & Norman 1998), which corresponds to all z for $\Omega_M = 0.3$.

The ideal method to follow would therefore be to mea-

sure cluster properties within radii corresponding to $\Delta_v(z)$ at all redshifts. This is not possible because X-ray measurements typically only extend to a fraction of the radius corresponding to $\Delta_v(z)$, even at low redshifts, requiring the extrapolation of measured properties by large factors. An alternative to this extrapolation is to work at a smaller radius, corresponding to a higher density contrast, $\Delta(0)$, at $z = 0$. In the self-similar model, this contrast will scale with redshift according to

$$\Delta(z) = \Delta(0) \frac{\Delta_v(z)}{\Delta_v(0)}. \quad (3)$$

In our analysis, all cluster properties are extrapolated to several different radii to enable comparison with other work. We note that for comparison with self-similar models, properties measured within a redshift-dependent density contrast are the most appropriate. In order to simplify the notation, integrated quantities with a numerical subscript, say $M_{\Delta(z)}$, refer to that quantity within a radius ($R_{\Delta(z)}$) enclosing a mean density of $\Delta(z)\rho_c(z)$. For example, $M_{200(z)}$ refers to the mass within a radius enclosing a mean overdensity of 200 at $z = 0$, and some higher mean overdensity (given by Equation 3) at higher redshifts. Note that this use of a redshift-dependent density contrast to define radii differs from the methods used in our previously published studies of some of these clusters. In Maughan et al. (2004a) and Maughan et al. (2004b), fixed (redshift-independent) density contrasts were used, while in Maughan et al. (2003) the virial radii were estimated from the temperatures of the clusters. The values of integrated cluster properties quoted in this paper thus differ from those given in the previous studies.

Under the self-similar model, with the assumptions that clusters are spherically symmetric systems and that they virialised at the redshift of observation (late formation), simple scaling relations between cluster properties can be derived, based on the virial theorem (*e.g.* Bryan & Norman 1998). The total gravitating mass within a radius $R_{\Delta(z)}$ is related to the gas temperature by

$$M_{\Delta(z)} E(z) \Delta(z)^{1/2} \propto kT^{3/2} \quad (4)$$

and the gas mass within $R_{\Delta(z)}$ is given by the relation,

$$M_g \Delta(z) E(z) \Delta(z)^{1/2} \propto kT^{3/2} f_{\text{gas}}. \quad (5)$$

If the relative distribution of gas and dark matter does not change with redshift or temperature, *i.e.* the gas-mass fraction f_{gas} is independent of z and kT , then Equation 5 becomes similar to Equation 4. This assumption is supported by measurements of f_{gas} in high-redshift clusters that are consistent with those in local clusters (*e.g.* Allen et al. 2002; Maughan et al. 2004a). However, it has been found that f_{gas} is lower in clusters with temperatures below $\sim 3 - 4$ keV (Sanderson et al. 2003, hereafter S03), which may invalidate the assumption of invariant f_{gas} for those systems.

Under the additional assumption that clusters emission is dominated by bremsstrahlung in the X-ray band (a reasonable assumption at the temperatures considered here), the X-ray luminosity within $R_{\Delta(z)}$ is given by

$$L_{\Delta(z)} E(z)^{-1} \Delta(z)^{-1/2} \propto kT^2 f_{\text{gas}}^2. \quad (6)$$

The scaling between total mass and X-ray luminosity (M – L relation) is then given by combining Equations 4

and 6, yielding

$$L_{\Delta(z)} E(z)^{-7/3} \Delta(z)^{-7/6} \propto M_{\Delta(z)}^{4/3} f_{\text{gas}}^2. \quad (7)$$

5 SUMMARY OF CLUSTER PROPERTIES AND LINE-FITTING METHODS

The methods used to derive the properties of the clusters in the sample can be summarised as follows. Overdensity radii $R_{\Delta(z)}$ were measured as described in §2. The luminosities measured within r_d were extrapolated to $R_{\Delta(z)}$ using the best-fitting surface-brightness profiles. The fractional detection radius $r_d/R_{200(z)}$ varied from 0.3 to 0.9, while $r_d/R_{2500(z)}$ was greater than unity for all clusters (see Table 1). The luminosities were thus scaled from r_d to $R_{200(z)}$ by factors in the range 1.0 – 1.5 (median = 1.1).

Similarly, the gas masses were derived at different $R_{\Delta(z)}$ by extrapolation of the gas-mass profiles, obtained from the surface-brightness profiles. The extrapolation factors of M_{gas} from r_d to $R_{200(z)}$ were in the range 1.1 – 5.3 with a median of 1.9. The total-mass profiles were used to derive the total masses at different overdensity radii, being scaled up by a factor in the range 1.1 – 3.8 (median = 1.7) from r_d to $R_{200(z)}$.

For ClJ0046.3+8530 and ClJ1226.9+3332, temperature profiles and hardness-ratio maps support the isothermal assumption to at least $0.6R_{200(z)}$. The effect of possible departures from isothermality is investigated below.

To enable comparisons with other work, the integrated properties of the WARPS sample are summarised in Table 2, derived within different radii.

The observed properties of the WARPS sample, and others, are compared with the predicted scaling relations in the following sections. The best-fitting scaling relations to the observations were found by performing an orthogonal, weighted ‘‘BCES’’ regression (as described by Akritas & Ber-shady 1996), on the data in log space. This method takes into account measurement errors on both variables, correlations in those errors, and intrinsic scatter in the data. The use of orthogonal regression avoids the biases inherent in bisector-regression fits to data with intrinsic scatter. The errors on the slopes and normalisations of the relations were derived from jackknife analyses of the datasets. The χ^2 goodness of fit values of the various relations were computed including the errors in both the x and y directions.

6 THE L – T RELATION

The effect of cool cores needs to be accounted for in any measurement of the L – T relation. Many relaxed clusters have dense cooling cores, with gas temperatures in the central ~ 100 kpc falling to $\sim 1/3$ of the global temperature, and sharply peaked surface-brightness profiles (*e.g.* Fabian 1994; Kaastra et al. 2001). These effects are not included in the self-similar model, so must be taken into account in the analysis. This is routinely done by excluding the central region of such clusters from the analyses. None of the clusters in our sample showed significant evidence for cooling cores; where temperature profiles and hardness-ratio maps could be created (ClJ0046.3+8530 and ClJ1226.9+3332) there was no indication of cooler gas in the central regions, and none

Cluster	z	kT keV	$R_{200(z)}$ Mpc	$L_{200(z)}$ $10^{44} \text{ erg s}^{-1}$	$M_{g, 200(z)}$ $10^{13} M_{\odot}$	$M_{200(z)}$ $10^{14} M_{\odot}$	$R_{2500(z)}$ Mpc	$L_{2500(z)}$ $10^{44} \text{ erg s}^{-1}$	$M_{g, 2500(z)}$ $10^{12} M_{\odot}$	$M_{2500(z)}$ $10^{13} M_{\odot}$
ClJ0046.3+8530	0.62	$4.4^{+0.5}_{-0.4}$	$0.95^{+0.06}_{-0.08}$	$4.16^{+0.24}_{-0.20}$	$3.69^{+0.38}_{-0.26}$	$2.75^{+0.59}_{-0.56}$	$0.24^{+0.02}_{-0.02}$	$2.04^{+0.40}_{-0.27}$	$3.78^{+0.96}_{-0.77}$	$5.22^{+1.46}_{-1.41}$
ClJ1342.9+2828 [†]	0.71	$3.7^{+0.6}_{-0.4}$	$0.88^{+0.07}_{-0.07}$	$3.52^{+0.16}_{-0.20}$	$3.08^{+0.35}_{-0.27}$	$2.45^{+0.62}_{-0.54}$	$0.18^{+0.02}_{-0.03}$	$1.50^{+0.38}_{-0.35}$	$2.27^{+0.87}_{-0.79}$	$2.85^{+1.30}_{-1.11}$
ClJ1113.1–2615	0.72	$4.1^{+0.5}_{-0.4}$	$0.90^{+0.06}_{-0.06}$	$4.14^{+0.32}_{-0.28}$	$2.88^{+0.27}_{-0.24}$	$2.77^{+0.59}_{-0.47}$	$0.24^{+0.02}_{-0.02}$	$2.77^{+0.25}_{-0.22}$	$4.44^{+0.70}_{-0.56}$	$6.10^{+1.46}_{-1.20}$
ClJ1103.6+3555 [†]	0.78	$5.0^{+0.7}_{-0.6}$	$0.89^{+0.06}_{-0.07}$	$4.66^{+0.23}_{-0.20}$	$3.59^{+0.36}_{-0.34}$	$2.82^{+0.65}_{-0.56}$	$0.21^{+0.02}_{-0.02}$	$1.95^{+0.30}_{-0.31}$	$3.00^{+0.76}_{-0.69}$	$4.77^{+1.52}_{-1.39}$
ClJ0152.7–1357N [†]	0.83	$5.3^{+0.7}_{-0.7}$	$0.97^{+0.09}_{-0.10}$	$11.70^{+1.41}_{-1.41}$	$6.45^{+1.15}_{-0.66}$	$3.97^{+1.28}_{-1.08}$	$0.14^{+0.04}_{-0.08}$	$2.27^{+1.62}_{-1.69}$	$1.36^{+1.83}_{-1.19}$	$1.37^{+2.02}_{-1.25}$
ClJ0152.7–1357S	0.83	$4.9^{+1.0}_{-0.9}$	$0.91^{+0.10}_{-0.11}$	$7.12^{+1.10}_{-0.92}$	$4.00^{+0.81}_{-0.62}$	$3.26^{+1.17}_{-1.02}$	$0.23^{+0.03}_{-0.04}$	$4.25^{+0.56}_{-0.63}$	$5.15^{+1.36}_{-1.43}$	$6.47^{+3.06}_{-2.55}$
ClJ1559.1+6353 [†]	0.85	$4.4^{+1.8}_{-1.1}$	$0.80^{+0.16}_{-0.13}$	$2.62^{+0.30}_{-0.29}$	$1.99^{+0.60}_{-0.38}$	$2.32^{+1.68}_{-0.96}$	$0.22^{+0.04}_{-0.04}$	$1.71^{+0.38}_{-0.44}$	$2.92^{+1.19}_{-1.02}$	$5.72^{+4.62}_{-2.49}$
ClJ1008.7+5342	0.87	$4.0^{+1.0}_{-0.7}$	$0.80^{+0.10}_{-0.11}$	$3.68^{+0.40}_{-0.29}$	$2.82^{+0.49}_{-0.38}$	$2.37^{+1.05}_{-0.81}$	$0.16^{+0.04}_{-0.05}$	$1.27^{+0.66}_{-0.62}$	$1.53^{+1.25}_{-0.99}$	$2.21^{+2.17}_{-1.40}$
ClJ1226.9+3332	0.89	$11.1^{+1.5}_{-1.4}$	$1.32^{+0.08}_{-0.10}$	$44.20^{+1.03}_{-1.05}$	$12.20^{+1.08}_{-0.98}$	$10.80^{+2.29}_{-2.10}$	$0.36^{+0.02}_{-0.03}$	$33.30^{+1.46}_{-1.61}$	$22.20^{+2.38}_{-2.67}$	$26.80^{+6.41}_{-5.39}$
ClJ1429.0+4241 [†]	0.92	$6.6^{+2.1}_{-1.2}$	$1.00^{+0.14}_{-0.12}$	$9.73^{+1.00}_{-0.89}$	$4.43^{+0.94}_{-0.67}$	$4.99^{+2.39}_{-1.58}$	$0.27^{+0.04}_{-0.04}$	$7.14^{+0.76}_{-0.81}$	$7.74^{+1.93}_{-1.72}$	$11.90^{+6.60}_{-4.19}$
ClJ1415.1+3612	1.03	$5.5^{+1.3}_{-0.8}$	$0.86^{+0.09}_{-0.09}$	$10.20^{+0.65}_{-0.63}$	$3.78^{+0.58}_{-0.45}$	$3.70^{+1.29}_{-0.98}$	$0.23^{+0.02}_{-0.03}$	$7.38^{+0.73}_{-0.84}$	$6.52^{+1.28}_{-1.32}$	$8.45^{+3.45}_{-2.65}$

Table 2. Summary of the integrated properties of the WARPS high-redshift sample derived within different radii. Luminosities are bolometric X-ray luminosities. [†]These systems show evidence of being unrelaxed, so were excluded from the analysis of the $M - T$ and $M_g - T$ relations.

of the surface-brightness profiles were centrally peaked. For this reason, no cooling-core correction was applied to the luminosities or temperatures of the high-redshift clusters.

If the $L - T$ relation evolves as predicted by Equation 6, then the effect of evolution can be removed by dividing the luminosity of each cluster by $E(z)^{-1}(\Delta(z)/\Delta(0))^{-1/2}$, which reduces to $E(z)^{-1}(\Delta_v(z)/\Delta_v(0))^{-1/2}$. Of the two factors describing the evolution, $E(z)$ dominates; at $z = 1$, $E(z)^{-1} = 0.57$ and $(\Delta_v(z)/\Delta_v(0))^{-1/2} = 0.80$. Fig. 4 shows the scaled luminosities (those with self-similar evolution factored out) measured within $R_{200(z)}$ plotted against temperature. A relation of the form

$$E(z)^{-1} \left(\frac{\Delta_v(z)}{\Delta_v(0)} \right)^{-1/2} L_{\Delta(z)} = A \left(\frac{kT}{6 \text{ keV}} \right)^B \quad (8)$$

was fit to the data, resulting in best-fit values $A = (5.3 \pm 1.6) \times 10^{44} h_{70}^{-2} \text{ erg s}^{-1}$, $B = 2.76 \pm 0.96$. The dot-dashed line in Fig. 4 shows the best-fitting relation with the *observed* luminosities, illustrating the effect of the predicted evolution.

Also plotted on Fig. 4 is the local $L - T$ relation measured by Arnaud & Evrard (1999, hereafter AE99) for a sample of clusters with little or no central cooling. It is unclear within what precise radius the AE99 luminosities were determined, however as they are referred to as “total luminosities” we assume they are derived within $R_{200(z)}$. If the AE99 luminosities were extrapolated to some larger radius (or to infinity), then the luminosities will be $\lesssim 10\%$ higher than the values within $R_{200(z)}$. The best fit to our scaled high-redshift data is consistent, within the errors, with the parameters for the local relation of $A = (5.86 \pm 0.40) \times 10^{44} h_{70}^{-2}$, $B = 2.88 \pm 0.15$. The local AE99 relation provides an acceptable fit to the scaled high-redshift data ($\chi^2/\nu = 5.6/9$), while the unscaled high-redshift data rule out the local relation ($\chi^2/\nu = 23.7/9$). We note that the slightly shallower slope in the WARPS data may have been influenced by the single point at 11.5 keV (ClJ1226.9+3332) in spite of the fact that the regression method attempts to account for intrinsic scatter within the data.

The scaled WARPS high- z $L - T$ relation is also compared with the local relation measured by Markevitch (1998) in Fig. 4. In contrast with AE99, Markevitch (1998) corrected for central cooling by excising the central regions of the clusters and extrapolating a surface-brightness profile

over this region. The luminosities measured by Markevitch (1998) were extrapolated to a fixed radius of $1.4h_{70}^{-1}$ Mpc, so are expected to be $\approx 2\%$ higher than the values derived within $R_{200(z)}$ (based on the typical scaling of luminosity from $1.4h_{70}^{-1}$ Mpc to $R_{200(z)}$ for our sample). The best-fitting relation found by Markevitch (1998) has $A = (6.35 \pm 0.55) \times 10^{44} h_{70}^{-2}$ and $B = 2.64 \pm 0.27$ in our notation. While the WARPS data are also consistent with this local relation ($\chi^2/\nu = 6.9/9$), we prefer to compare the results with AE99 because their treatment of central cooling is consistent with ours.

6.1 Comparison with the Vikhlinin et al. (2002)

The results for the WARPS sample was compared with those obtained by Vikhlinin et al. (2002, hereafter V02) for a sample consisting of 22 clusters at $z > 0.4$ observed with *Chandra*. In the V02 sample, luminosities were extrapolated to a fixed radius of $1.4h_{70}^{-1}$ Mpc irrespective of their redshift. In order to compare the V02 luminosities with self-similar predictions, they were scaled to $R_{200(z)}$. The value of $R_{200(z)}$ was computed in an identical way to the WARPS clusters (see §2) using the values of z , kT , r_c and β given by V02. Random realisations of the overdensity profiles were computed from the uncertainties on z , kT , β , given by V02. The luminosity of each system was then scaled from $1.4h_{70}^{-1}$ Mpc to $R_{200(z)}$ based on β -profiles with the parameters given by V02 for that cluster. The resulting scale factors for the luminosities were close to unity, ranging from 0.89 to 1.02 with a mean of 0.98.

As no errors on L_X are given by V02, the mean fractional uncertainty from the WARPS sample of 0.09 was assumed for the V02 clusters. The errors on the luminosities scaled to $R_{200(z)}$ thus include the statistical uncertainties in modeling the overdensity profiles, and an additional 9% uncertainty.

V02 excluded the central $71h_{70}^{-1}$ kpc of clusters which had peaked surface-brightness profiles, and extrapolated over that region to correct for central cooling effects. As no cooling corrections were applied to the WARPS clusters, the corrected clusters were discarded from the V02 sample. We also excluded ClJ0152.7–1357, which is already in the WARPS sample, leaving 13 V02 clusters. The best-fitting $L - T$ relation for those clusters was consistent with the

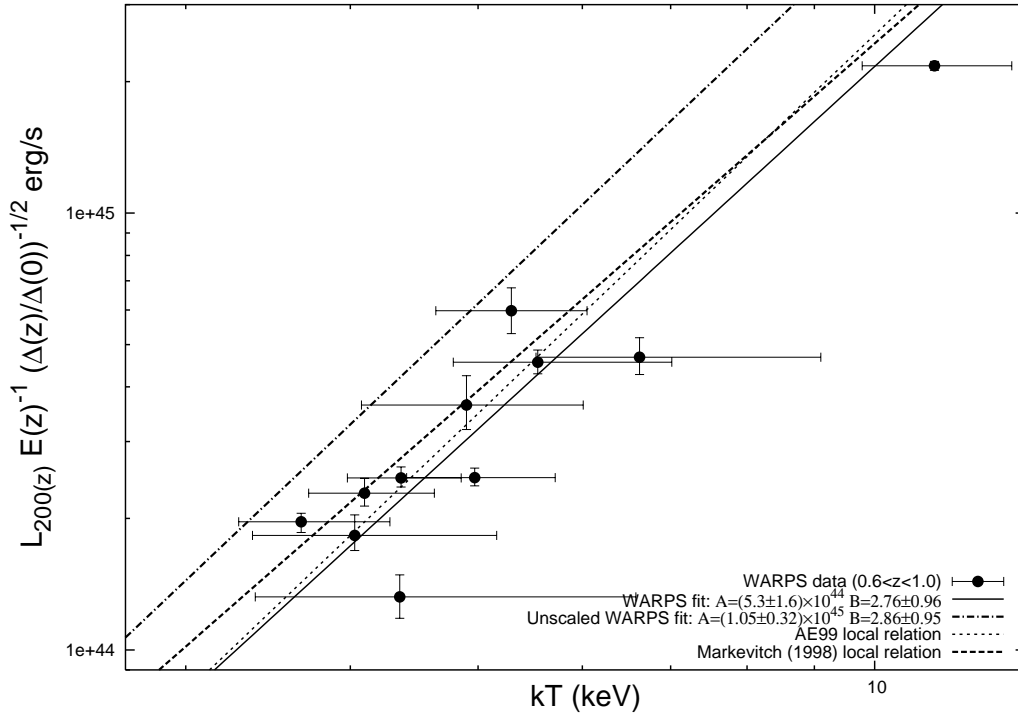


Figure 4. L – T relation for the high-redshift WARPS sample. Luminosities were extrapolated to a radius $R_{200(z)}$, corresponding to a redshift-dependent density contrast 200, and scaled by a factor of $E(z)^{-1}[\Delta(z)/\Delta(0)]^{-1/2}$ as predicted by the self-similar model. The solid line is the best fit to the data, and the dotted and dashed lines are the local relations of AE99 and Markevitch (1998) respectively

WARPS L – T relation shown in Fig. 4. The two samples were then combined to give a sample of 22 systems, with 16 at $z > 0.6$. The luminosities were scaled as before to remove the predicted self-similar evolution, and the resulting L – T relation is shown in Fig. 5, along with the local AE99 relation.

The best-fitting parameters for the joint sample are $A = (6.34 \pm 0.65) \times 10^{44} h_{70}^{-2}$ and $B = 3.29 \pm 0.38$. This is consistent with the local AE99 relation at the 90% level, with $\chi^2/\nu = 28.6/22$. Comparison of the *unscaled* data for the combined WARPS and V02 samples (indicated by the dot-dashed line in Fig. 5) with the AE99 relation strongly rules out the local relation as a description of the high-redshift data ($\chi^2/\nu = 135/22$).

As the WARPS results are based mainly on *XMM-Newton* observations, a potential source of systematic error is that cooling cores in high-redshift systems could go undetected due to the large PSF of *XMM-Newton*. However, the best-fitting relation for the combination of the WARPS sample and the V02 data (excluding the systems with cooling cores detected by *Chandra*) is a good description of both samples (Fig. 5). Both samples also show a similar amount of scatter about the best-fitting relation. This suggests that the *XMM-Newton* measurements were not contaminated by undetected cooling cores.

6.2 Comparison with Ettori et al. (2004)

The WARPS sample was then compared with the larger, more recently compiled sample of Ettori et al. (2004, hereafter E04) which comprises 28 clusters at $z > 0.4$ from the

Chandra archive. In E04, luminosities were extrapolated to $R'_{500(z)}$, where the prime indicates a slightly different definition of $\Delta(z)$ used in that work. The density contrast in E04 was defined as

$$\Delta'(z) = 500 \frac{\Delta_v(z)}{18\pi^2}, \quad (9)$$

so is related to our $\Delta(z)$ by

$$\Delta'(z) = \frac{\Delta_v(0)}{18\pi^2} \Delta(z). \quad (10)$$

In the case of an Einstein-de Sitter universe $\Delta'(z) = \Delta(z)$. In our assumed low-density Λ CDM cosmology however, $\Delta_v(0)/18\pi^2 = 1.76$ and so $\Delta'(z) < \Delta(z)$, leading to higher measured luminosities within $R'_{500(z)}$. This change in definition thus introduces a redshift-independent change in all luminosities, but the predicted evolution of the L – T relation is unaffected. For consistency with E04, the luminosities of the WARPS clusters were extrapolated to $R'_{500(z)}$. The resulting WARPS L – T relation is plotted along with the E04 relation in Fig. 6. The AE99 relation is also plotted for comparison, though it should be recalled that those luminosities were extrapolated to larger radii. In addition to any evolution, the normalisation of the AE99 relation should thus be $\approx 5\%$ higher than the $R'_{500(z)}$ relations (estimated from the extrapolation of a standard β -profile from $R'_{500(z)}$ to $R_{200(z)}$).

The best fit to the WARPS $R'_{500(z)}$ L – T relation is consistent with the $R_{200(z)}$ relation of Fig. 4, and the local AE99 relation (see Table 3). The best fit to the E04 relation, with $A = (5.2 \pm 1.0) \times 10^{44} h_{70}^{-2}$ and $B = 4.25 \pm 0.61$, is possibly steeper than the other L – T relations discussed

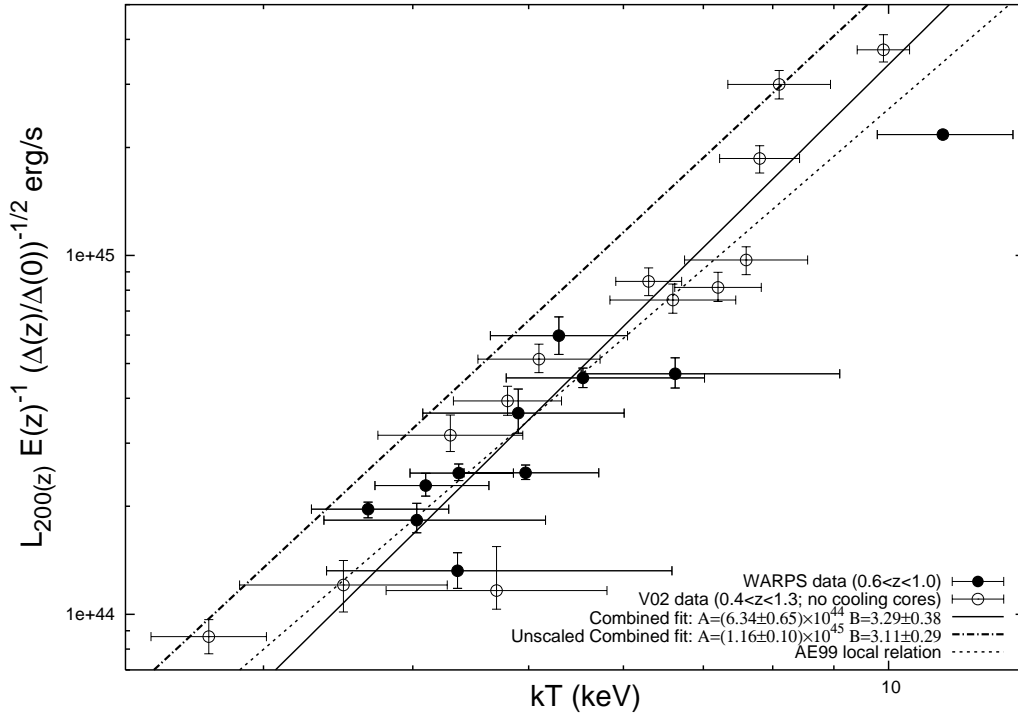


Figure 5. $L - T$ relation for the combined WARPS and V02 samples. The WARPS data are the same as in Fig. 4. The V02 data were treated in the same way, with L_X extrapolated to $R_{200(z)}$ and scaled by $E(z)^{-1}[\Delta(z)/\Delta(0)]^{-1/2}$. The solid line is the best fit to the combined dataset.

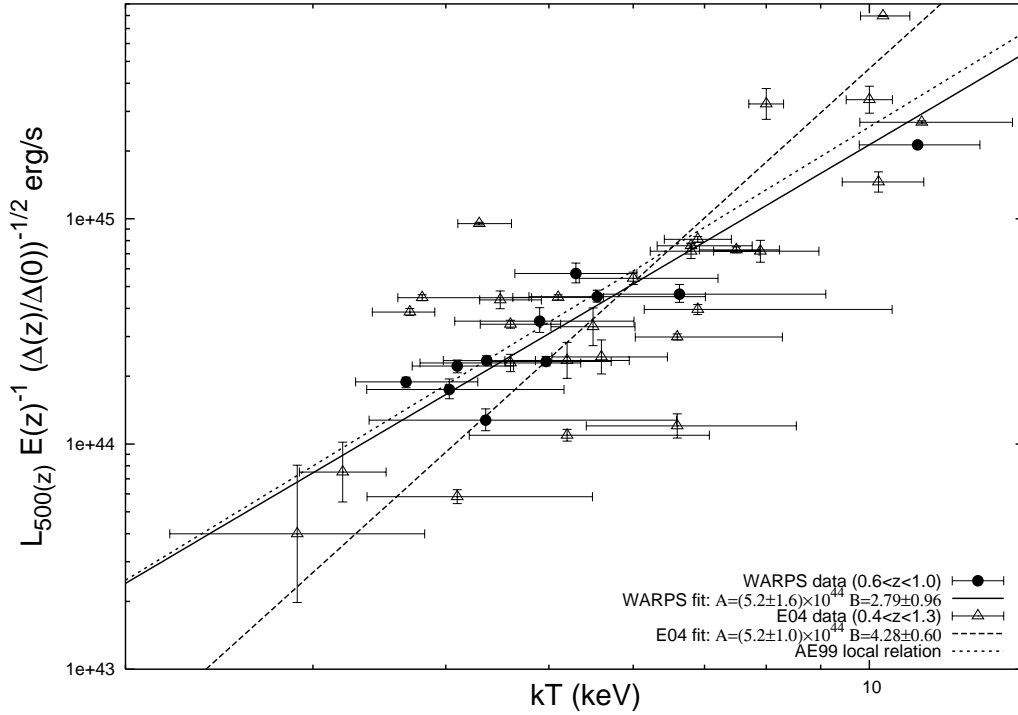


Figure 6. $L - T$ relations of the WARPS and E04 samples. Luminosities were extrapolated to $R'_{500(z)}$.

here (at the $\sim 2\sigma$ level). The data also show larger scatter about the best-fitting relation. We note that the slope we measure for the E04 sample is steeper than that quoted in E04 ($B = 3.72 \pm 0.47$). This is because we have scaled the luminosities by $E(z)^{-1}(\Delta_v(z)/\Delta_v(0))^{-1/2}$ whereas E04 scaled by $E(z)^{-1}$ alone, and because we use an orthogonal BCES regression, while E04 used a bisector BCES regression. If we eliminate these two differences, we recover the same fit as E04.

The E04 sample is a superset of the V02 sample, but shows larger scatter, and a possibly steeper L – T relation. The difference is not caused by the different extraction radii used in the two samples, as the WARPS L – T relation is relatively unaffected by the use of different outer radii. One difference between the E04 and V02 data is that E04 made no corrections for cooling cores. To investigate the importance of this, we removed the clusters that were classified as having cooling cores by V02 from the E04 sample. We also removed most of the clusters that were not in the V02 sample, as the presence of cooling cores in those systems is unknown. However we retained the two systems (ClJ1113.1–2615 and ClJ1226.9+3332) that are also in our sample, and show no evidence for cooling cores. The best-fitting L – T relation for this ‘no cooling core’ subsample of the E04 data is given in Table 3. The scatter about the relation is somewhat reduced by the exclusion of possible cooling-core systems, and the slope is in slightly better agreement with the other L – T relations (mainly due to its increased uncertainty).

Four clusters in our sample are included in the E04 sample. The temperatures and luminosities measured by us were consistent (within 1σ) with those found by E04 with the following exceptions. E04 measured temperatures for ClJ1113.1–2615 and ClJ0152.7–1357S that were 1.9σ and 1.6σ higher than our measurements, respectively. The luminosity of ClJ1226.9+3332 measured by E04 was 2.2σ higher than our measurement. The reasons for these differences is not clear, although they are not strongly significant.

Given the large scatter in the E04 sample, and the good agreement between the WARPS and V02 L – T relations, we prefer to use the combined WARPS and V02 L – T relation, with luminosities measured within $R_{200(z)}$ in our further discussions. The different L – T relations discussed in this section are summarised in Table 3.

7 THE M – T RELATION

In the self-similar evolution scenario, assuming the late-formation approximation, the M – T relation is given by Equation 4. The evolution of the M – T relation was investigated by comparing the WARPS sample to the local sample of S03, which comprises 66 clusters with reliable masses derived from temperature and surface-brightness profiles. We chose S03 for this comparison because the overdensity radii and mass measurements were made in the same way as in this work. S03 also derived total and gas masses for their sample under the often incorrect assumption of isothermality. Those isothermal masses are extremely useful in making a fair comparison with the high-redshift data, separating the systematic effects of assuming isothermality from any evolution. For consistency with the WARPS sample, we include only the 40 clusters from the S03 sample with $kT > 3$ keV.

The slopes and normalisations of the relations we fit to the S03 data vary from those reported in S03 because of this temperature cut-off, and because we use a slightly different fitting algorithm than S03.

A reliable masses measurement requires that the clusters be spherically symmetric and in hydrostatic equilibrium. The five possibly unrelaxed high-redshift clusters (ClJ1342.9+2828, ClJ1103.6+3555, ClJ0152.7–1357N, ClJ1559.1+6353 and ClJ1429.0+4241) were thus excluded from these measurements of the M – T relation.

Masses were derived within $R_{2500(z)}$, which falls within the detection radius for all of the WARPS clusters, and $R_{200(z)}$, which corresponds to the estimated virial radius used in many other studies. Similarly to the method used with the L – T relation, the predicted self-similar evolution was factored out of the high-redshift cluster masses by fitting a relation of the form

$$E(z) \left(\frac{\Delta_v(z)}{\Delta_v(0)} \right)^{1/2} M_{\Delta(z)} = A \left(\frac{kT}{6 \text{ keV}} \right)^B \quad (11)$$

to the data.

Fig. 7 shows the $M_{2500(z)}$ – T relation for the S03 and WARPS samples. The masses for both samples were derived assuming isothermality. The temperatures of the S03 clusters are emission-weighted temperatures measured within $0.3R_{200(z)}$, which corresponds closely to $R_{2500(z)}$, and are extrapolated over any central cool gas (see S03). The WARPS temperatures are also emission weighted, and are measured within the clusters’ detection radii. These measurements are consistent, under the assumption of isothermality, with the S03 temperature measurements. Our best-fitting relation for the S03 data is given by $A = (1.92 \pm 0.10) \times 10^{14} h_{70}$ and $B = 1.89 \pm 0.15$, while the best-fit to the WARPS data is parameterised by $A = (1.67 \pm 0.32) \times 10^{14} h_{70}$ and $B = 1.78 \pm 0.48$.

While the S03 isothermal masses plotted in Fig. 7 provide the fairest comparison with the high-redshift data available, the most reliable masses are those derived using the temperature profiles of the clusters. The dotted line plotted in Fig. 7 shows the best fit for local clusters whose masses were derived using temperature profiles (the best-fit parameters given in Table 4). The assumption of isothermality makes no significant difference to the M – T relation within $R_{2500(z)}$.

The $M_{2500(z)}$ – T relation was also measured for the WARPS systems when their masses were not scaled by the predicted evolution, and is plotted as a dot-dashed line in Fig. 7. These unscaled masses provide strong evidence for evolution of the $M_{2500(z)}$ – T relation; the χ^2 of the isothermal local relation to the unscaled high-redshift data is $\chi^2/\nu = 17.7/4$. The *scaled* high-redshift data agree well with the local isothermal relation, with $\chi^2/\nu = 1.3/4$. We note that ClJ1008.7+5342 at 4 keV is $\approx 1\sigma$ below the best-fitting relation, which may be due to the system not being fully relaxed (§3).

The $M_{200(z)}$ – T relation is shown in Fig. 8 for the S03 and WARPS samples. The temperatures of the S03 clusters are as above, but measured within $R_{200(z)}$, while the WARPS temperatures are again measured within r_d . The isothermal S03 masses were used and the best-fit parameters are summarised in Table 4. Again, the scaled high-redshift data are consistent with the local isothermal rela-

L – T relation	A ($10^{44} h_{70}^{-2}$ erg s $^{-1}$)	B	notes
Luminosities extrapolated to $R_{200}(z)$			
AE99	5.86 ± 0.40	2.88 ± 0.15	Local clusters with no strong central cooling (Fig. 4).
Markevitch (1998)	6.35 ± 0.55	2.64 ± 0.27	Local relation, corrected for cooling cores (Fig. 4).
WARPS	5.3 ± 1.6	2.76 ± 0.96	$0.6 < z < 1.0$ clusters with no cooling cores (Fig. 4).
V02 & WARPS	6.34 ± 0.65	3.29 ± 0.38	Combined samples ($0.4 < z < 1.3$), no cooling cores (Fig. 5).
Luminosities extrapolated to $R'_{500}(z)$			
E04	5.2 ± 1.0	4.25 ± 0.61	Full E04 $0.4 < z < 1.3$ sample (Fig. 6).
E04 (no cool cores)	3.9 ± 1.0	4.20 ± 0.98	E04 $0.4 < z < 1.3$ clusters with no cooling cores.
WARPS ($R'_{500}(z)$)	5.2 ± 1.6	2.79 ± 0.96	WARPS $0.6 < z < 1.0$ clusters with no cooling cores (Fig. 6).

Table 3. Summary of the L – T relations discussed in §6. Luminosities of the high-redshift clusters were scaled by $E(z)^{-1}(\Delta_v(z)/\Delta_v(0))^{-1/2}$ to remove the predicted self-similar evolution.

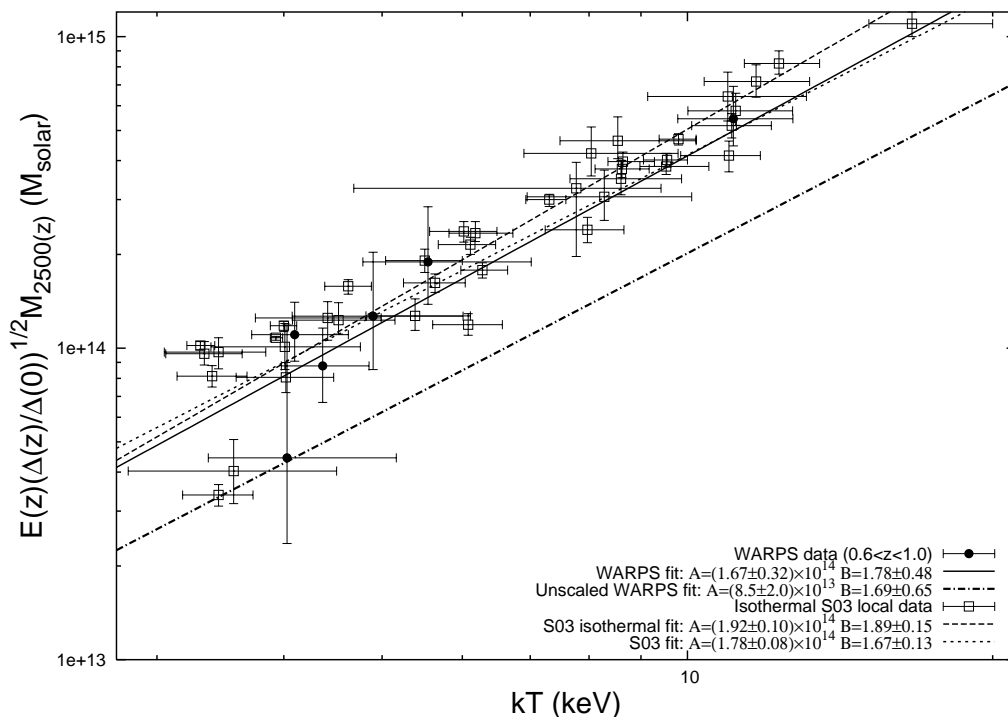


Figure 7. $M_{2500}(z)$ – T relation for the low- z S03 clusters and the relaxed high- z WARPS systems. Masses were measured within $R_{2500}(z)$ assuming isothermality and scaled by the evolution predicted by the self-similar model. The dotted line shows the best fit to the S03 data when the masses are derived using the measured temperature profiles, rather than assuming isothermality. The best-fitting relation to the high-redshift data when the masses are not scaled by the predicted evolution is shown with the dot-dashed line.

tion ($\chi^2/\nu = 1.6/4$), however they are inconsistent with the local relation when the reliable masses derived from temperature profiles are used ($\chi^2/\nu = 10.5/4$). This is because, as noted by S03, assuming isothermality leads to a systematic overestimate of the total mass within R_{200} .

The best-fitting relation for the WARPS data using masses not scaled by the predicted evolution is also plotted in Fig. 8 as a dot-dashed line. The unscaled high-redshift data are inconsistent with the local isothermal $M_{200}(z)$ – T relation ($\chi^2/\nu = 21.2/4$), providing evidence for evolution. However, we note that the unscaled WARPS data are consistent with the local relation using masses derived from temperature profiles ($\chi^2/\nu = 3.0/4$), because the mass overestimate in the high-redshift systems due to assuming isothermality almost cancels with the predicted self-similar evolu-

tion. This highlights the importance of properly quantifying the systematic effects of assuming isothermality when investigating the evolution of cluster masses.

To enable comparisons with other work, masses of the WARPS clusters were also derived within radii enclosing fixed, redshift-independent density contrasts of $\Delta(z) = \Delta(0) = 2500$ and $\Delta(z) = \Delta(0) = 200$. These data were then fit with a relation of the form

$$M_{\Delta(z)} = A \left(\frac{kT}{6 \text{ keV}} \right)^B, \quad (12)$$

so no scaling for the predicted self-similar evolution was made. The best-fitting slopes and normalisations are given in Table 4. The agreement between these M – T relations and the isothermal S03 relations are much worse than when

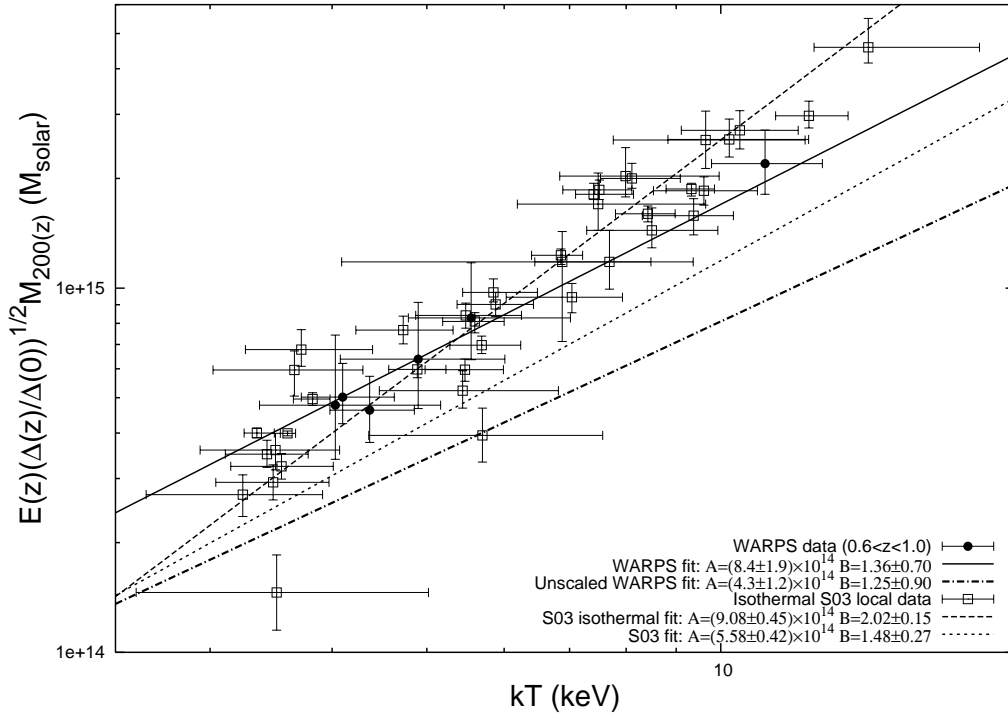


Figure 8. $M_{200(z)} - T$ relation for the low- z S03 clusters and the relaxed high- z WARPS systems. Masses were measured within $R_{200(z)}$ assuming isothermality and scaled by the evolution predicted by the self-similar model. The dotted line shows the best fit to the S03 data when the masses are derived using the measured temperature profiles, rather than assuming isothermality. The best-fitting relation for the high-redshift data when the masses are not scaled by the predicted evolution is shown with the dot-dashed line.

redshift-*dependent* density contrasts were used. The isothermal S03 relations are poor descriptions of these unscaled high-redshift relations, with χ^2 probabilities of $\leq 1\%$.

8 THE $M_g - T$ RELATION

The comparison of the WARPS and S03 samples also enabled the investigation of the evolution of the $M_g - T$ relation. The gas mass is less dependent on uncertainties in the cluster temperature structure than the total mass. This is because the gas density profile is obtained easily from the X-ray surface-brightness profile, and the gas luminosity depends strongly on density (as ρ^2) and weakly on temperature (as $T^{1/2}$). This makes the $M_g - T$ relation potentially a more reliable method of exploring cluster evolution. The incorrect assumption of isothermality will still introduce systematic effects because the definition of overdensity radii depends on the total mass profile. The self-similar $M_g - T$ evolution prediction (Equation 5) is also subject to additional assumptions about the relative distributions of the gas and dark matter (§4).

The $M_g - T$ relations of the S03 and WARPS samples were derived within $R_{2500(z)}$ and $R_{200(z)}$, and are plotted in Figs. 9 and 10 respectively. The predicted self-similar evolution was again factored out of the high-redshift cluster gas masses, with a relation of the form

$$E(z) \left(\frac{\Delta_v(z)}{\Delta_v(0)} \right)^{1/2} M_{g, \Delta(z)} = A \left(\frac{kT}{6 \text{ keV}} \right)^B \quad (13)$$

fit to the data. As with the $M - T$ relation, only the re-

laxed clusters in our sample were included in this analysis (*i.e.* ClJ1342.9+2828, ClJ1103.6+3555, ClJ0152.7-1357N, ClJ1559.1+6353 and ClJ1429.0+4241 were excluded). $M_g - T$ relations were fit to the S03 data, using their gas masses derived under the incorrect assumption of isothermality, and the more reliable masses derived using temperature profiles. Table 5 summarises the parameters of the various best-fitting relations.

Measured within $R_{2500(z)}$, the scaled high-redshift and isothermal low-redshift $M_g - T$ relations are consistent, with $\chi^2/\nu = 2.5/4$. ClJ1008.7+5342 falls slightly below the relation, as it did in the $M - T$ relation measured within this radius (Fig. 7). The assumption of isothermality has no significant effect on the local relation.

The scaled high-redshift $M_g - T$ relation within $R_{200(z)}$ is also consistent with the S03 isothermal relation ($\chi^2/\nu = 4.1/4$), and in poor agreement with the local relation with masses derived from temperature profiles ($\chi^2/\nu = 9.7/4$). This demonstrates that the systematic effects of assuming isothermality are important in the $M_{g, 200(z)} - T$ relation.

The $M_g - T$ relations for the WARPS clusters when the masses were not scaled by the predicted self-similar evolution are plotted as dot-dashed lines in Figs. 9 and 10. Within both radii, the unscaled high-redshift data are strongly inconsistent with the local isothermal relations, demonstrating the evolution of the relations.

V02 also investigated the evolution of the $M_g - T$ relation, measuring gas masses within an overdensity radius defined in terms of the average baryon density of the universe. Although their measurements are not directly comparable

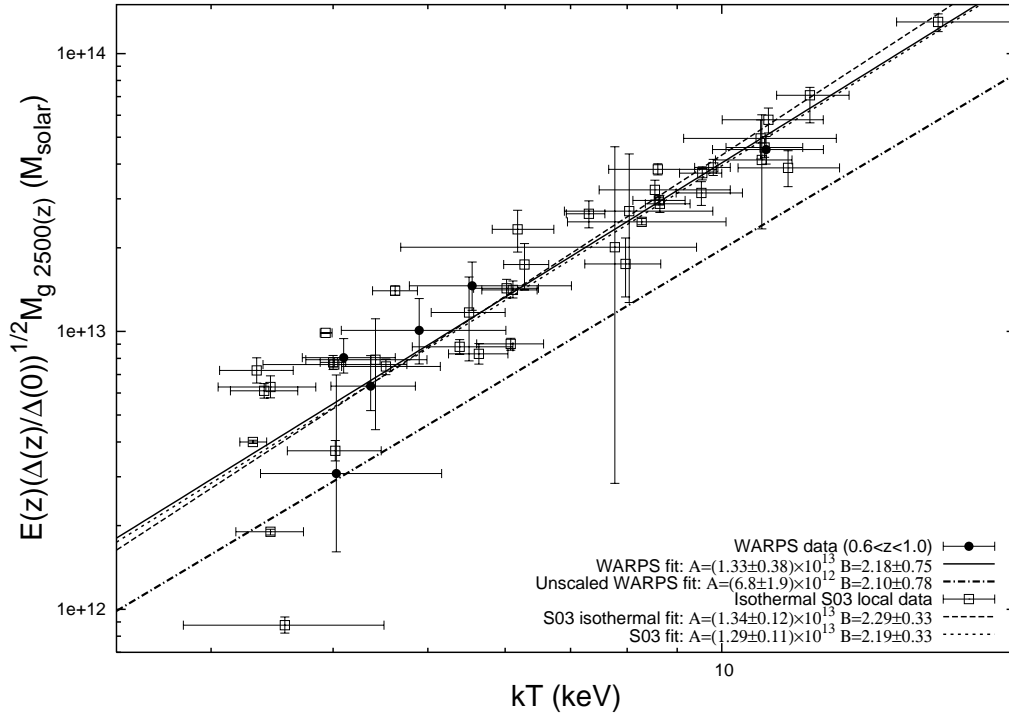


Figure 9. The $M_{g, 2500(z)} - T$ relations of the low- z S03 clusters and relaxed, high- z WARPS systems. Masses were measured within $R_{2500(z)}$ assuming isothermality, and scaled by the evolution predicted by the self-similar model. The dotted line shows the best fit to the S03 data when the masses are derived using temperature profiles. The best-fitting relation to the high-redshift data when the masses are not scaled by the predicted evolution is shown with the dot-dashed line.

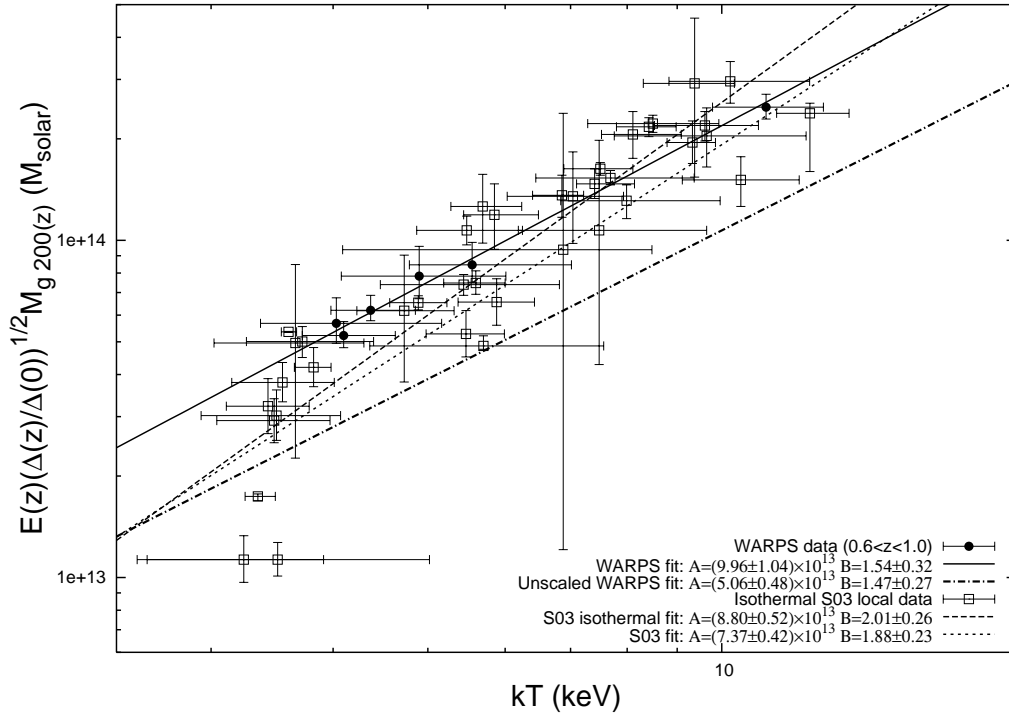


Figure 10. The $M_{g, 200(z)} - T$ relations of the low- z S03 clusters and relaxed, high- z WARPS systems. Masses were measured within $R_{200(z)}$ assuming isothermality, and scaled by the evolution predicted by the self-similar model. The dotted line shows the best fit to the S03 data when the masses are derived using temperature profiles. The best-fitting relation to the high-redshift data when the masses are not scaled by the predicted evolution is shown with the dot-dashed line.

M – T relation	A ($10^{14} h_{70}^{-1} M_{\odot}$)	B	notes
Masses within $R_{2500(z)}$			
WARPS $M_{2500(z)} - T$	1.67 ± 0.32	1.78 ± 0.48	$0.6 < z < 1.0$ clusters assuming isothermality (Fig. 7).
S03 $M_{2500(z)} - T$	1.78 ± 0.08	1.67 ± 0.13	Local clusters with measured kT profiles (Fig. 7).
S03 $M_{2500(z)} - T$	1.92 ± 0.10	1.89 ± 0.15	Local clusters with incorrect assumption of isothermality (Fig. 7).
Masses within $R_{200(z)}$			
WARPS $M_{200(z)} - T$	8.4 ± 1.9	1.36 ± 0.70	$0.6 < z < 1.0$ clusters assuming isothermality (Fig. 8).
S03 $M_{200(z)} - T$	5.58 ± 0.42	1.48 ± 0.27	Local clusters with measured kT profiles (Fig. 8).
S03 $M_{200(z)} - T$	9.08 ± 0.45	2.02 ± 0.15	Local clusters with incorrect assumption of isothermality (Fig. 8).
Unscaled masses within redshift-independent density contrast			
WARPS $M_{2500} - T$	1.20 ± 0.34	1.49 ± 0.85	$0.6 < z < 1.0$ clusters assuming isothermality.
WARPS $M_{200} - T$	5.3 ± 1.5	1.26 ± 0.88	$0.6 < z < 1.0$ clusters assuming isothermality.

Table 4. Summary of the M – T relations discussed in §7. Masses of the high-redshift clusters were scaled by $E(z)(\Delta_v(z)/\Delta_v(0))^{1/2}$ to remove the predicted self-similar evolution, with the exception of the bottom section of the table.

$M_g - T$ relation	A ($10^{13} h_{70}^{-1} M_{\odot}$)	B	notes
Gas masses within $R_{2500(z)}$			
WARPS $M_g 2500(z) - T$	1.33 ± 0.38	2.18 ± 0.75	$0.6 < z < 1.0$ clusters assuming isothermality (Fig. 9).
S03 $M_g 2500(z) - T$	1.29 ± 0.11	2.19 ± 0.33	Local clusters with measured kT profiles (Fig. 9).
S03 $M_g 2500(z) - T$	1.34 ± 0.12	2.29 ± 0.33	Local clusters with incorrect assumption of isothermality (Fig. 9).
Gas masses within $R_{200(z)}$			
WARPS $M_g 200(z) - T$	9.96 ± 1.04	1.54 ± 0.32	$0.6 < z < 1.0$ clusters assuming isothermality (Fig. 10).
S03 $M_g 200(z) - T$	7.37 ± 0.42	1.88 ± 0.23	Local clusters with measured kT profiles (Fig. 10).
S03 $M_g 200(z) - T$	8.80 ± 0.52	2.01 ± 0.26	Local clusters with incorrect assumption of isothermality (Fig. 10).

Table 5. Summary of the $M_g - T$ relations discussed in §8. Masses of the high-redshift clusters were scaled by $E(z)(\Delta_v(z)/\Delta_v(0))^{1/2}$ to remove the predicted self-similar evolution.

to ours for this reason, they find evidence for weak evolution in the $M_g - T$ relation, qualitatively consistent with our results.

9 THE M – L RELATION

The scaling between total mass and X-ray luminosity in the high-redshift clusters was then investigated. The WARPS sample was compared with the low-redshift HIFLUGCS sample of Reiprich & Böhringer (2002) in order to measure any evolution in the M – L relation. The masses and luminosities published in Reiprich & Böhringer (2002) were scaled to $H_0 = 70 \text{ km s}^{-1} \text{ Mpc}^{-1}$, and clusters with $kT < 3 \text{ keV}$ were removed for consistency with the WARPS clusters, leaving 52. The HIFLUGCS sample includes systems regardless of their morphology, although any strong sub-structure was excluded for the mass and luminosity determinations, so all of the high-redshift clusters are included in this comparison (*i.e.* ClJ1342.9+2828, ClJ1103.6+3555, ClJ0152.7–1357N, ClJ1559.1+6353 and ClJ1429.0+4241 were included). In addition, the masses of the local systems were determined assuming isothermality, which enables a fair comparison with the high-redshift masses. Properties extrapolated to R_{200} were used, and a relation of the form

$$E(z)^{-7/3} \left(\frac{\Delta_v(z)}{\Delta_v(0)} \right)^{-7/6} L_{200(z)} = A \left(\frac{M_{200(z)}}{5 \times 10^{14} h_{70}^{-1} M_{\odot}} \right)^B$$

was fit to high- and low-redshift data separately.

Fig. 11 shows the best-fitting M – L relations for the two samples, and the parameters of the different relations are summarised in Table 6. The dot-dashed line shows the best-fitting M – L relation when no scaling for the predicted evolution is applied. The disagreement between that unscaled high- z relation and the local data is striking, even given the large scatter in the local data. However, when the high-redshift data are scaled by the predicted evolution, the best-fitting relation (solid line) agrees very well with the local relation (dashed line), with $\chi^2/\nu = 4.9/9$. The slopes of the low- and high- z relations are consistent, and are both steeper than the self-similar prediction of $4/3$ (although not significantly for the high- z data). At least some of the larger scatter in the HIFLUGCS data is due to cooling cores in some systems, as no correction for these was made (Reiprich & Böhringer 2002).

10 DISCUSSION

The normalisation of the WARPS high-redshift scaling relations are all consistent with self-similar evolution of the local relations in a Λ CDM cosmology. We emphasise the importance of properly quantifying the effect of assuming isothermality on the derived masses of high-redshift clusters when investigating the evolution of the M – T relations. The L – T and $M_g 2500(z) - T$ relations are the most robust of the high-redshift relations measured here, subject to the smallest systematic uncertainties and extrapo-

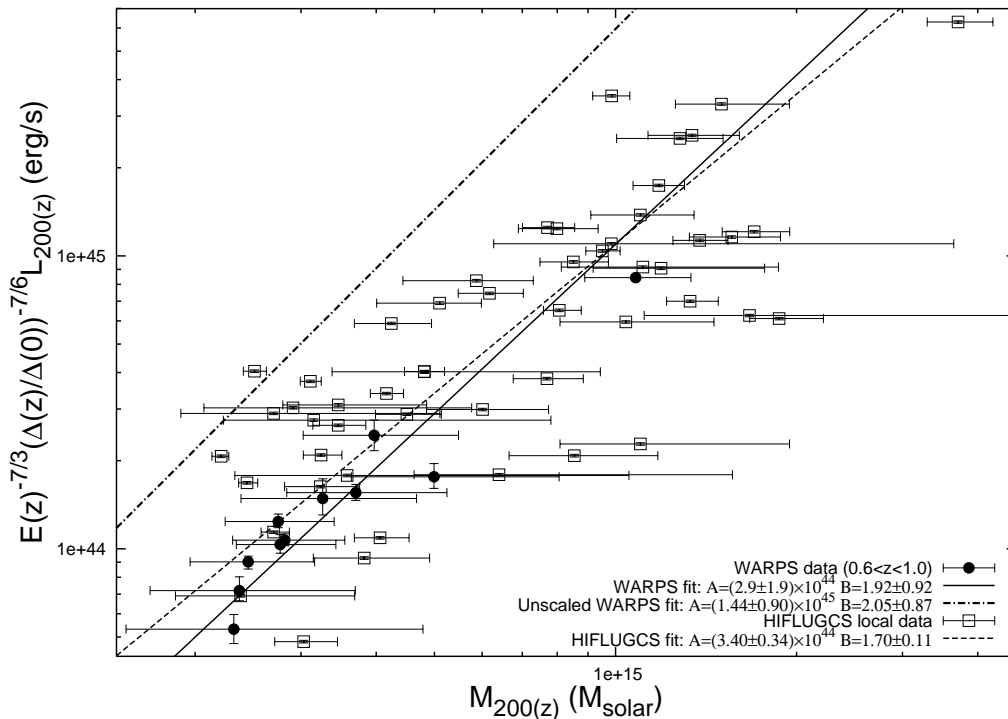


Figure 11. $M - L$ relation for the low- z HIFLUGCS clusters and the high- z WARPS systems. Masses were measured within $R_{200(z)}$ assuming isothermality and luminosities within the same radius were scaled by the evolution predicted by the self-similar model. The best-fitting relation to the high-redshift data when the luminosities are not scaled by the predicted evolution is shown with the dot-dashed line.

$M - L$ relation	A ($10^{44} h_{70}^{-2}$ erg s $^{-1}$)	B	notes
Properties within $R_{200(z)}$			
WARPS $M - L$	2.9 ± 1.9	1.92 ± 0.92	$0.6 < z < 1.0$, luminosities scaled for predicted evolution (Fig. 11).
Unscaled WARPS $M - L$	15.8 ± 6.6	1.84 ± 0.54	$0.6 < z < 1.0$, no scaling for predicted evolution (Fig. 11).
HIFLUGCS $M - L$	3.40 ± 0.34	1.70 ± 0.11	Local clusters assuming isothermality (Fig. 11).

Table 6. Summary of the $M - L$ relations discussed in §9.

lations. In particular the combined V02 and WARPS high- z sample enable the $L - T$ relation to be measured with relatively small uncertainties. The $M - L$ relation meanwhile is predicted to show the strongest evolution ($\propto E(z)^{-7/3}(\Delta_v(z)/\Delta_v(0))^{-7/6}$). The consistency of these relations with the predicted self-similar evolution provides strong evidence that that model is a good description of cluster evolution out to $z \approx 1$.

A preliminary measurement of the high-redshift $M_{2500(z)} - T$ relation in Maughan et al. (2003) found that it was consistent with no evolution, but did not strongly rule out self-similar evolution. This work improves on that earlier study in several ways. The sample used is larger, and the latest calibration was used in reanalysing the *Chandra* data (see §2). An important difference is that the masses are measured within radii corresponding to redshift-dependent density contrasts, estimated from the overdensity profile of each system. In the earlier study, the masses were measured within a fraction of the virial radius estimated from each cluster’s temperature. The current study thus pro-

vides a more reliable measurement of the evolution of the $M_{2500(z)} - T$ relation.

The slope of the combined WARPS and V02 $L - T$ relation is consistent with its low-redshift counterparts, and steeper than the slope of 2 predicted by the self-similar model. A possible interpretation of this is that the same non-gravitational processes are affecting the high-redshift clusters as those in the local universe. This would place a lower limit of $z \approx 1$ on the epoch of non-gravitational contributions to clusters. An alternative interpretation is that the non-gravitational effects are important during the early stages of clusters’ lives, regardless of redshift, as the clusters discussed here are generally relaxed in appearance, suggesting the major part of their formation is complete. The high-redshift $M - L$ relation also supports this interpretation.

The slopes of $M_{200(z)} - T$ relation above 3 keV in both the WARPS and S03 samples are consistent with the self-similar prediction of 3/2. When the cooler S03 systems are included, the slope steepens, which is consistent with non-gravitational effects having a larger relative contribution in low-mass systems. Observations of cooler (< 3 keV)

clusters at high-redshift are required to test whether there is any evolution in this effect. There is a weak trend for the $M_{2500(z)} - T$ and $M_g - T$ relations to be steeper than the $M_{200(z)} - T$ and $M_g - T$ relations, whose slopes agree more closely with the self-similar slope. This trend is present, though not strongly significant, in the high- and low-redshift relations. These results are consistent with a scenario in which non-gravitational processes have a stronger effect in the central regions of clusters, which is more noticeable in cooler systems.

Generally, the $M - T$ relations show a self-similar slope above 3 keV, the $M_g - T$ relations are self-similar, or slightly steeper, and the $L - T$ relations are steeper than self-similar prediction. This suggests that although non-gravitational processes do not have a strong influence on the dark matter in > 3 keV clusters, those processes can still have an important effect on the gas in more massive systems.

10.1 Evolution of the $L - T$ relation

As we saw in the §6, the evolution of the $L - T$ relation is consistent with the self-similar model described in §4. The relatively large size of the combined WARPS and V02 samples enables different models of cluster evolution to be tested. As discussed in section §4, it is popular to use a fixed, redshift-independent density contrast to define the outer radius of clusters. In this case, the $L - T$ relation is given by

$$L_{\Delta} E(z)^{-1} \propto kT^B. \quad (15)$$

Now the $\Delta(z)^{-1/2}$ part of the normalisation is no longer required, and as this is an increasing function of z , the predicted $L - T$ evolution is smaller than that predicted by the $\Delta(z)$ model. The measured luminosities are slightly larger when extrapolated to R_{Δ} instead of $R_{\Delta(z)}$, which acts in the opposite sense, increasing the apparent evolution. This evolution model was tested by comparing the combined WARPS and V02 $L - T$ relation, with luminosities extrapolated to R_{200} (not $R_{200(z)}$) and scaled by $E(z)^{-1}$, with the local AE99 relation. The $E(z)^{-1}$ scaling was insufficient to reduce the luminosities to be consistent with the local $L - T$ relation, with $\chi^2/\nu = 51/22$.

A simple way of measuring the evolution of the $L - T$ relation is to assume that it evolves as

$$L_{\Delta} \propto (1+z)^{\alpha} kT^B. \quad (16)$$

V02 found $\alpha = 1.5 \pm 0.3$ at 90% confidence by comparing their high-redshift data with the local Markevitch (1998) $L - T$ relation. The combined WARPS and V02 $L - T$ data were used to make a similar measurement. The luminosity of each cluster extrapolated to R_{200} was scaled by $(1+z)^{-\alpha}$, and the scaled data were compared with a local relation. This process was performed for a range of values of α , and for both of the local AE99 and Markevitch (1998) $L - T$ relations and the results are shown in Fig. 12.

We find the best agreement between the scaled high-redshift data and the local AE99 relation, with $\alpha = 1.4 \pm 0.2$ (at the 90% level) and $\chi^2/\nu = 23.0/22$. Using the Markevitch (1998) relation as a low-redshift baseline results in a slightly lower value of α and a poorer fit. A measurement of α independent of that of V02 was also performed by using the WARPS sample alone. Compared with the AE99 local relation we find $\alpha = 1.1 \pm 0.3$ while comparison with

the Markevitch (1998) relation gives $\alpha = 0.9 \pm 0.3$ (see Fig. 13). These measurements are consistent with the value of $\alpha = 1.5 \pm 0.3$ found by Lumb et al. (2004) in a sample of 8 high-redshift clusters observed with *XMM-Newton*. We thus conclude that $\alpha \approx 1.2$ and that the range of values found is at least partially due to the uncertainty in the exact form of the local $L - T$ relation.

Recent theoretical work has attempted to include the effects of preheating and radiative cooling in the simple self-similar scaling relations. Voit (2005) shows that introducing a cooling threshold $K_c = T^{2/3} t(z)^{2/3}$, where gas with an entropy less than K_c radiates all of its thermal energy away within a Hubble time $t(z)$, produces a “cooling threshold” $L - T$ relation of the form

$$L \propto kT^{2.5} E(z)^{-1} t(z)^{-1}. \quad (17)$$

Voit (2005) also investigates the effect that including a modest initial amount of entropy in the gas before it is accreted onto a forming cluster has on the $L - T$ relation. If the initial entropy level is chosen to match the observation that $K(0.1R_{200}) \propto kT^{2/3}$ (Ponman et al. 2003), then the resulting “altered similarity” $L - T$ relation is

$$L \propto kT^3 E(z)^{-3} t(z)^{-2}. \quad (18)$$

Both of these modified self-similar models predict $L - T$ slopes which are in better agreement with observations than the simple self-similar slope of 2. The evolution of the $L - T$ relation, however, is much milder in the modified self-similar models than in the simple self-similar model. Fig. 14 shows the evolution of the normalisation of the $L - T$ relation for a variety of models. The data points show the observed evolution in the combined WARPS and V02 sample relative to the AE99 and Markevitch (1998) local relations. The data are binned by redshift, and the data points show the weighted mean and its associated error for each bin. Luminosities measured within R_{200} (not $R_{200(z)}$) were used, but as discussed above, the exact choice of luminosity radius has little effect on the measured evolution. Fig. 15 shows the same information, but without binning, illustrating the scatter within each bin. While the binned representation is pushing the limits of the data, and the scatter within each bin is large, Figs. 14 and 15 serve to illustrate the range of predictions for the evolution of the $L - T$ relation, and more importantly that the evolution predicted by the modified self-similar models is weaker than that observed.

10.2 Continuous formation predictions

The $M - T$ relation defined in Equation 4 is derived under the late-formation approximation, in which a cluster forms in a single collapse, terminating with the system having just virialised at the redshift of observation. Several authors (*e.g.* Lacey & Cole 1993; Voit 2000) have derived $M - T$ relations in a more realistic continuous-formation scenario, in which clusters grow by accumulating much smaller virialised objects. In a flat Λ CDM cosmology, Voit (2000) predicts

$$kT = (8.0 \text{ keV}) \left(\frac{M}{10^{15} h_{100}^{-1} M_{\odot}} \right)^{2/3} \frac{\xi_c(t)}{\xi_c(t_0)} \quad (19)$$

where $\xi_c(t)$ is the specific energy of a shell of matter which collapses onto the cluster at a time t (see the appendix of

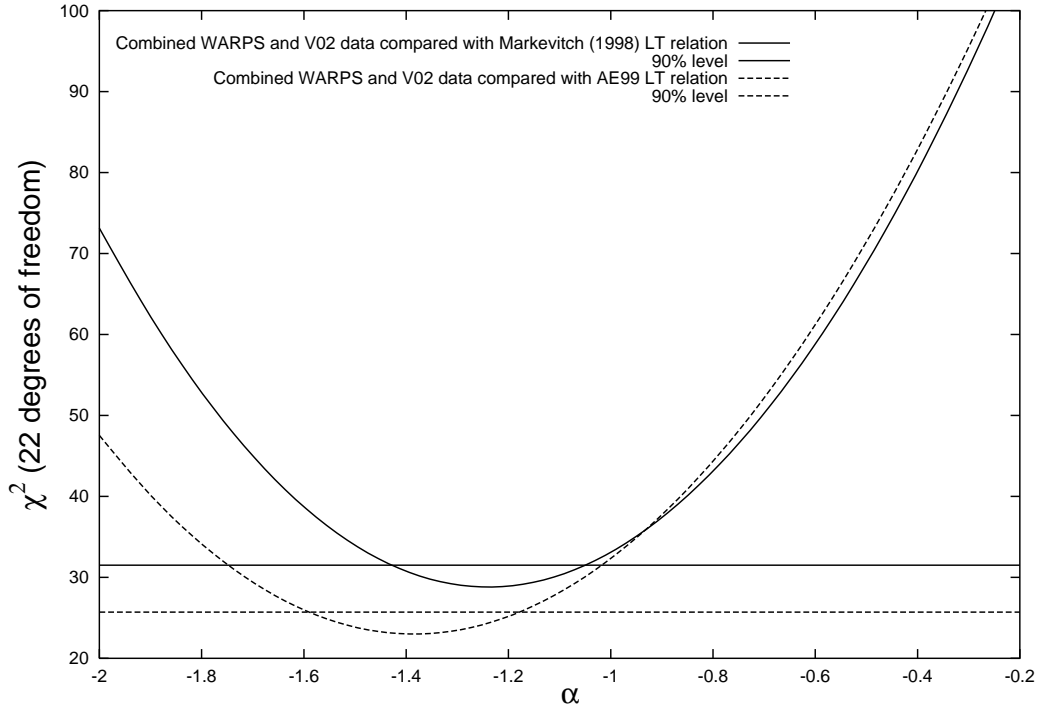


Figure 12. The χ^2 values for the comparison of the scaled high-redshift WARPS and V02 L – T data with the local relations. The luminosities of the high-redshift systems were scaled by $(1+z)^{-\alpha}$ for different values of α .

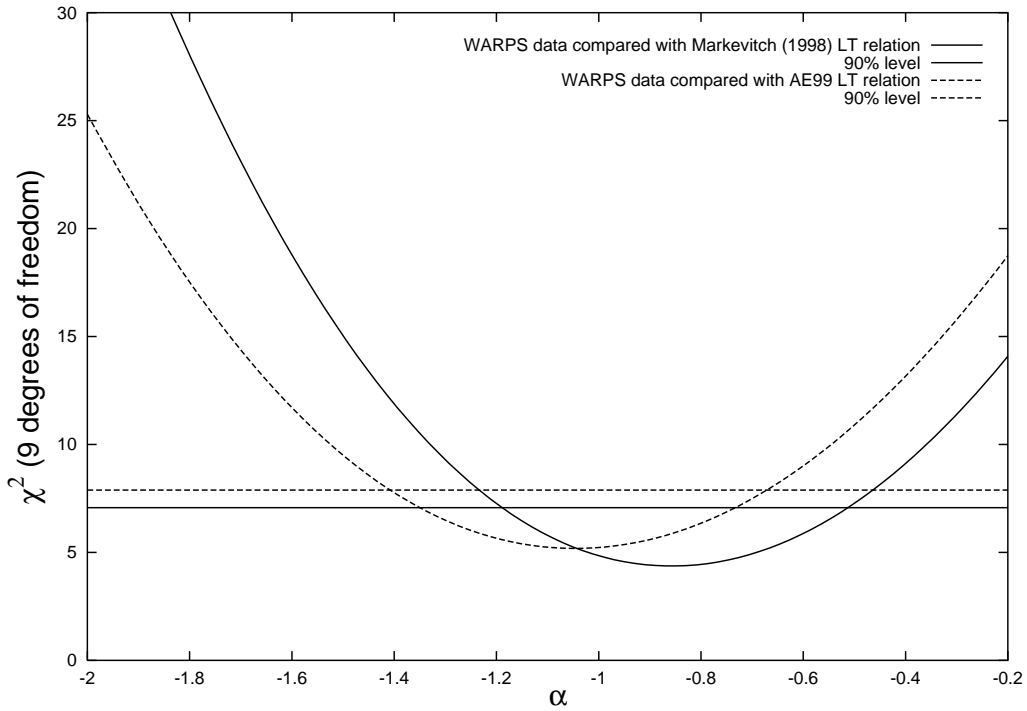


Figure 13. The χ^2 values for the comparison of the scaled high-redshift WARPS L – T data alone with the local relations. The luminosities of the high-redshift systems were scaled by $(1+z)^{-\alpha}$ for different values of α .

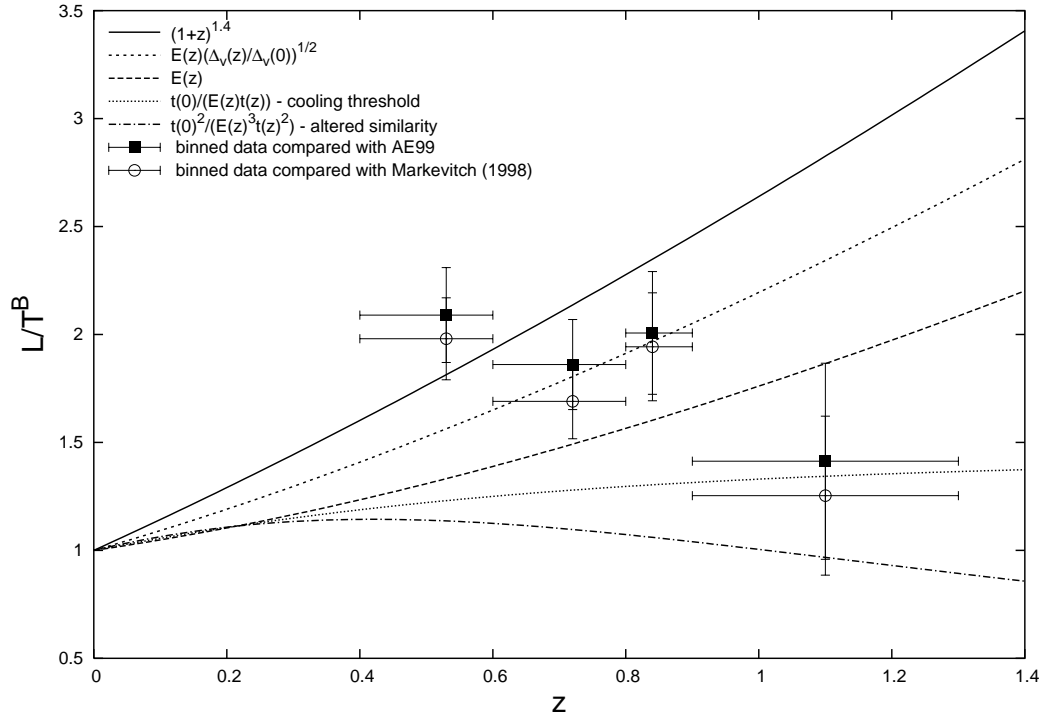


Figure 14. The evolution of the L – T relation normalisation predicted by different models. The data points are the observed evolution in the combined WARPS and V02 sample, in redshift bins, relative to different local L – T relation.

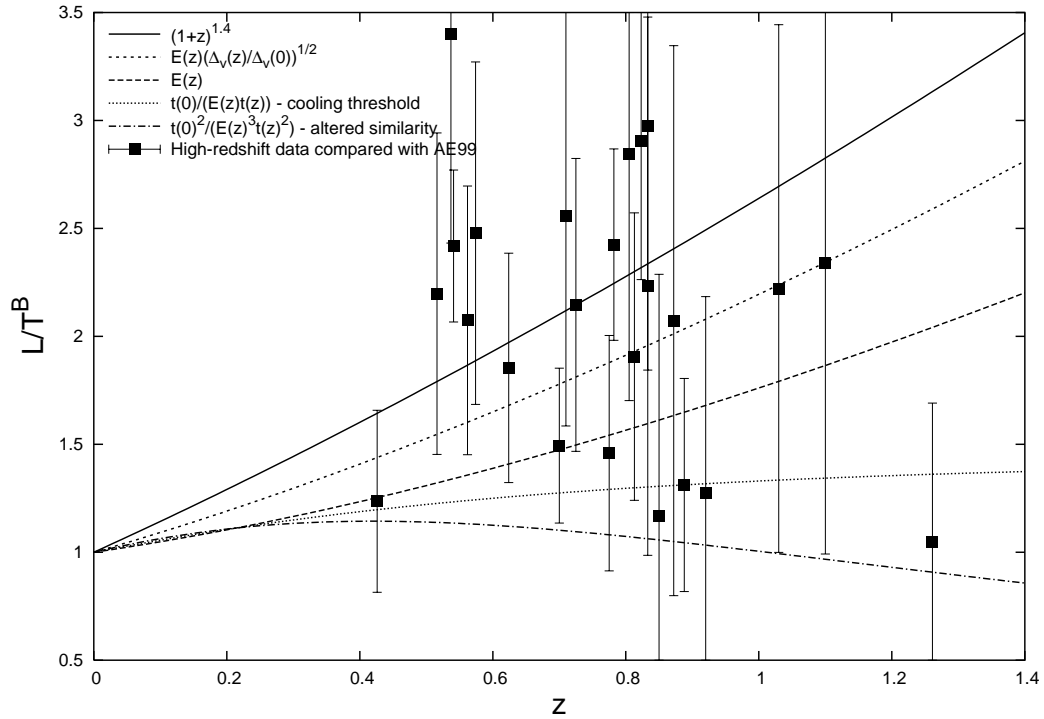


Figure 15. The evolution of the L – T relation normalisation predicted by different models. The data points are the observed evolution in the combined WARPS and V02 sample relative to different local L – T relation.

Voit 2000 for details). In this model, the evolution of the normalisation of the $M - T$ relation is different from the late-formation predictions.

The continuous-formation model predicts that clusters of a given mass are cooler than the late-formation model predictions. However, the difference between the models is small at $z \approx 1$, requiring measurements of the $M - T$ normalisation to a precision of $< 2\%$ to distinguish between them, and our results are consistent with either of these cluster-formation scenarios. The agreement between our measurements of the evolution of the $M - T$ and $M_g - T$ relations, and these models indicates that the properties of galaxy clusters reflect the properties of the universe at their redshift of observation. In the late-formation approximation this is simply because clusters formed at the redshift of observation, while in the continuous-formation model, the accretion of matter onto clusters continually realigns their properties with those of the evolving universe.

10.3 Probing the redshift of virialisation

If clusters form in a single collapse, then they may virialise at a redshift (z_v) which is larger than their redshift of observation (z_{obs}). Their properties would then reflect those of the universe at an epoch earlier than z_{obs} , and the self-similar evolution which assumes $z_{\text{obs}} = z_v$ would not be a good description of the high-redshift scaling relations. If one is willing to assume that clusters obey self-similar evolution, then the high-redshift data can be used to place interesting constraints on the mean redshift of formation of the high-redshift sample (z_{vh}). If the mean redshift of formation of the local sample is denoted as z_{vl} , then the normalisation of the $L - T$ relation increases with redshift by a factor $[E(z_{\text{vh}})\Delta_v(z_{\text{vh}})^{1/2}]/[E(z_{\text{vl}})\Delta_v(z_{\text{vl}})^{1/2}]$.

Under the assumptions given above, the ratio of the normalisations of the high- and low-redshift $L - T$ relations can be used to relate z_{vl} and z_{vh} . The high-redshift $L - T$ relation thus allows z_{vh} to be measured for an assumed z_{vl} . Figure 16 shows the constraints on z_{vh} from the combined WARPS and V02 high- z $L - T$ relation, using the AE99 relation as a low- z baseline. The error bars are 99% errors derived from the maximum and minimum normalisation of the high-redshift $L - T$ relation allowed by the high-redshift data at the 99% level.

If the local or high-redshift clusters formed at a redshift other than z_{obs} , then the overdensity radii within which the luminosities are measured would be inappropriate. However, as the overdensity radii are all large and the surface-brightness is low in outer regions of the clusters, the use of different radii has a negligible effect. To illustrate this, if we consider a 6 keV cluster with $\beta = 0.67$ and $r_c = 100$ kpc observed at $z = 0$, we find $R_{200(z)} = 2.0$ Mpc for $z_v = 0$ and $R_{200(z)} = 1.6$ Mpc for $z_v = 1$. The luminosity of the cluster increases by just 1% between these two radii.

Figure 16 shows that if the local clusters are assumed to have virialised at $z = 0$, then the high-redshift data are consistent with $z_{\text{vh}} = z_{\text{obs}}$, with $z_{\text{vh}} < 1.5$ at the 99% level. We strongly rule out a common redshift of virialisation for the local and high-redshift samples, regardless of the redshift of formation of the local sample.

10.4 Properties of the WARPS clusters

The observed gas properties of the WARPS high-redshift sample are generally consistent with those of local clusters. The mean surface-brightness profile slope, $\beta = 0.66 \pm 0.05$ is very close to the canonical value of $2/3$. Also, the mean ratio of core radius to “virial radius” $r_c/R_{200(z)} = 0.15 \pm 0.06$ agrees well with the values found by Sanderson & Ponman (2003) for > 1 keV clusters. Furthermore, the gas-mass fractions found in the high-redshift clusters agree with those found in local clusters. The weighted mean f_{gas} at $R_{2500(z)}$ is 0.073 ± 0.010 , increasing to 0.12 ± 0.02 at $R_{200(z)}$ which agrees with the values found by S03. These results indicate that the gas distribution is the same in low- and high-redshift clusters.

The metal abundances measured in the high-redshift systems are plotted against redshift in Fig. 17. The data (excluding ClJ1559.1+6353 with its very high, poorly constrained measurement) are consistent with the canonical value of $0.3Z_{\odot}$ out to $z = 1$; the weighted mean of the values is $0.28 \pm 0.16Z_{\odot}$. This is consistent with the high-redshift of enrichment of the intra-cluster medium found by other authors (*e.g.* Mushotzky & Loewenstein 1997; Tozzi et al. 2003).

11 CONCLUSIONS

The overall picture provided by this study of the evolution of the cluster scaling relations is that within the statistical limits of the current data, the evolution of galaxy clusters out to $z \approx 1$ is described well by the self-similar model. The large-scale properties of clusters are dominated by the density of the universe at the epoch at which they are observed.

12 ACKNOWLEDGEMENTS

We thank Alastair Sanderson for providing us with properties at different radii for the S03 sample. We are grateful to Stephen Helsdon for providing some of the software used for the regression line fitting. BJM was supported for the majority of this work by a Particle Physics and Astronomy Research Council (PPARC) postgraduate studentship. BJM is currently supported by NASA through Chandra Postdoctoral Fellowship Award Number PF4-50034 issued by the Chandra X-ray Observatory Center, which is operated by the Smithsonian Astrophysical Observatory for and on behalf of NASA under contract NAS8-03060. HE gratefully acknowledges financial support from NASA grant NAG 5-10085.

REFERENCES

- Akritas M. G., Bershady M. A., 1996, ApJ, 470, 706
- Allen S. W., Schmidt R. W., Fabian A. C., 2002, MNRAS, 334, L11
- Arnaud M., Aghanim N., Neumann D. M., 2002, A&A, 389, 1
- Arnaud M., Evrard A. E., 1999, MNRAS, 305, 631
- Bower R. G., 1997, MNRAS, 288, 355
- Bryan G. L., Norman M. L., 1998, ApJ, 495, 80

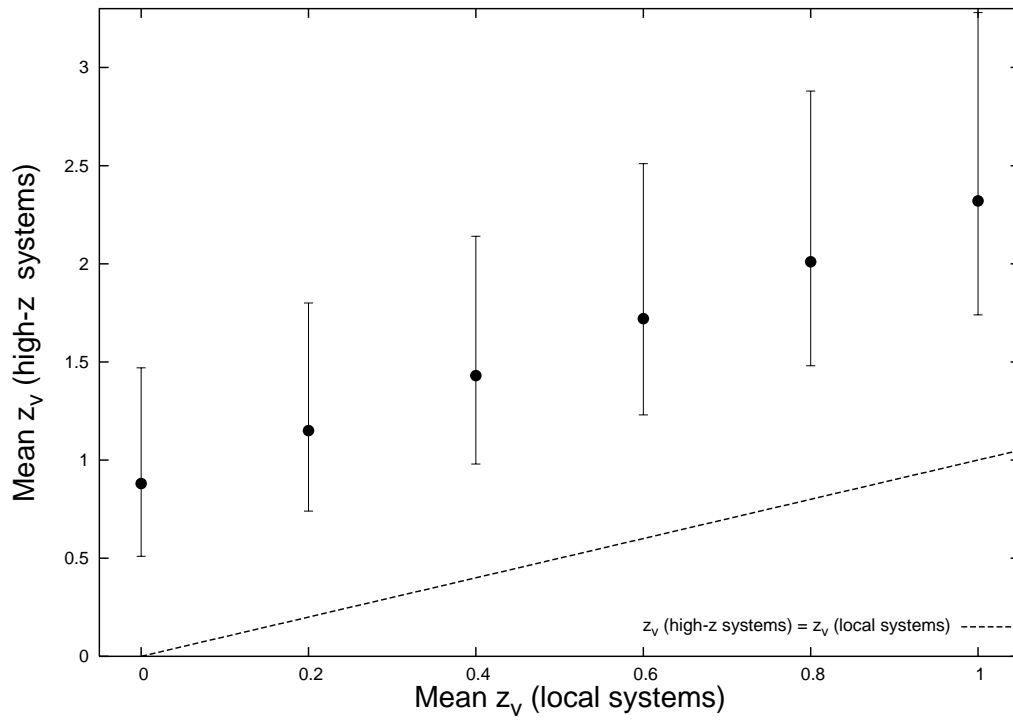


Figure 16. Constraints on the mean redshift of virialisation of the combined WARPS and V02 high-redshift sample derived from the evolution of the L – T relation. The dotted line indicates a common redshift of virialisation of the high- and low-redshift samples. Errorbars are 99%.

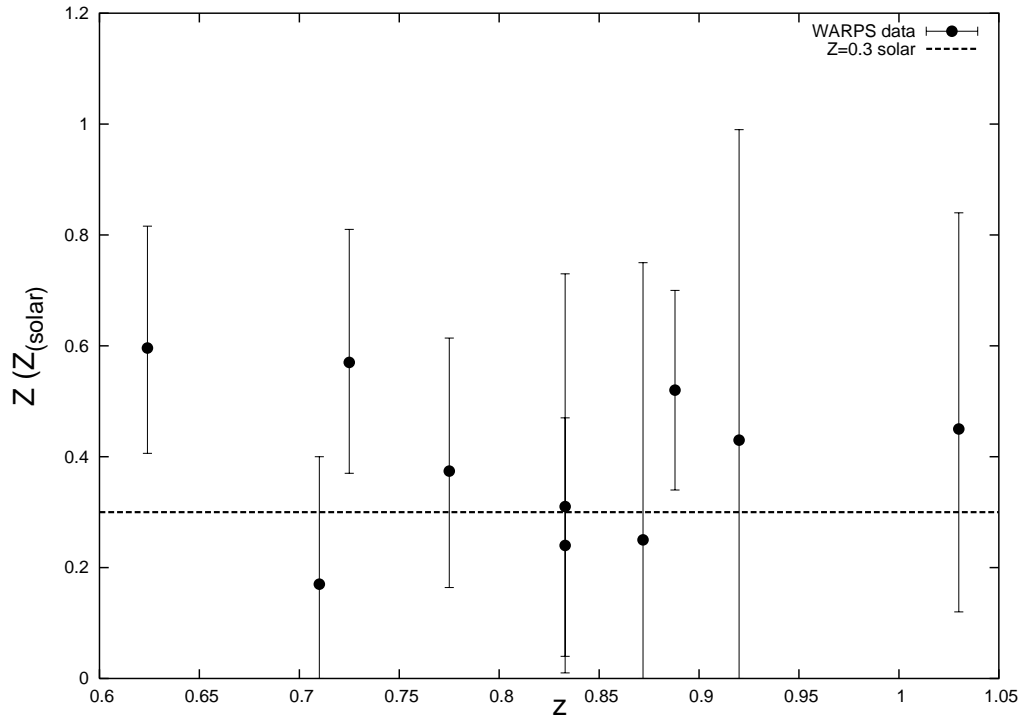


Figure 17. Cluster metallicity plotted against redshift for the WARPS high-redshift sample. Note that the poorly constrained high metallicity value measured in CLJ1559.1+6353 is not included in this plot.

- Cagnoni I., Elvis M., Kim D.-W., Mazzotta P., Huang J.-S., Celotti A., 2001, *ApJ*, 560, 86
- Cavaliere A., Fusco-Femiano R., 1976, *A&A*, 49, L137
- Dickey J. M., Lockman F. J., 1990, *ARA&A*, 28, 215
- Donahue M., Voit G. M., Scharf C. A., Gioia I. M., Mullis C. R., Hughes J. P., Stocke J. T., 1999, *ApJ*, 527, 525
- Ebeling H., Jones L. R., Perlman E., Scharf C., Horner D., Wegner G., Malkan M., Fairley B., Mullis C. R., 2000, *ApJ*, 534, 133
- Ettori S., Tozzi P., Borgani S., Rosati P., 2004, *A&A*, 417, 13
- Fabian A. C., 1994, *ARA&A*, 32, 277
- Fairley B. W., Jones L. R., Scharf C., Ebeling H., Perlman E., Horner D., Wegner G., Malkan M., 2000, *MNRAS*, 315, 669
- Huo Z., Xue S., Xu H., Squires G., Rosati P., 2004, *AJ*, 127, 1263
- Jee M. J., White R. L., Benítez N., Ford H. C., Blakeslee J. P., Rosati P., Demarco R., Illingworth G. D., 2005, *ApJ*, 618, 46
- Kaastra J. S., Ferrigno C., Tamura T., Paerels F. B. S., Peterson J. R., Mittaz J. P. D., 2001, *A&A*, 365, L99
- Kaastra J. S., Mewe R., 1993, *A&AS*, 97, 443
- Lacey C., Cole S., 1993, *MNRAS*, 262, 627
- Lloyd-Davies E. J., Ponman T. J., Cannon D. B., 2000, *MNRAS*, 315, 689
- Lumb D. H., Bartlett J. G., Romer A. K., Blanchard A., Burke D. J., Collins C. A., Nichol R. C., Giard M., Marty P. B., Nevalainen J., Sadat R., Vauclair S. C., 2004, *A&A*, 420, 853
- Markevitch M., 1998, *ApJ*, 504, 27
- Markevitch M., Vikhlinin A., 2001, *ApJ*, 563, 95
- Maughan B. J., Jones L. R., Ebeling H., Perlman E., Rosati P., Frye C., Mullis C. R., 2003, *ApJ*, 587, 589
- Maughan B. J., Jones L. R., Ebeling H., Scharf C., 2004, *MNRAS*, 351, 1193
- Maughan B. J., Jones L. R., Lumb D., Ebeling H., Gondoin P., 2004, *MNRAS*, 354, 1
- Mushotzky R. F., Loewenstein M., 1997, *ApJ*, 481, L63
- Mushotzky R. F., Scharf C. A., 1997, *ApJ*, 482, L13
- Perlman E. S., Horner D. J., Jones L. R., Scharf C. A., Ebeling H., Wegner G., Malkan M., 2002, *ApJS*, 140, 265
- Ponman T. J., Cannon D. B., Navarro J. F., 1999, *Nature*, 397, 135
- Ponman T. J., Sanderson A. J. R., Finoguenov A., 2003, *MNRAS*, 343, 331
- Reiprich T. H., Böhringer H., 2002, *ApJ*, 567, 716
- Sanderson A. J. R., Ponman T. J., 2003, *MNRAS*, 345, 1241
- Sanderson A. J. R., Ponman T. J., Finoguenov A., Lloyd-Davies E. J., Markevitch M., 2003, *MNRAS*, 340, 989
- Scharf C., Jones L. R., Ebeling H., Perlman E., Malkan M., Wegner G., 1997, *ApJ*, 477, 79
- Tozzi P., Rosati P., Ettori S., Borgani S., Mainieri V., Norman C., 2003, *ApJ*, 593, 705
- Vikhlinin A., VanSpeybroeck L., Markevitch M., Forman W. R., Grego L., 2002, *ApJ*, 578, L107
- Voit G. M., 2000, *ApJ*, 543, 113
- Voit G. M., 2005, *Reviews of Modern Physics*, 58, 1